

Can tides explain the low dark matter density in Fornax?

Anna Genina,^{1,2*} Justin I. Read,³ Azadeh Fattahi,² Carlos S. Frenk²

¹ *Max-Planck-Institut für Astrophysik, Karl-Schwarzschild-Str. 1, D-85748, Garching, Germany*

² *Institute for Computational Cosmology, Department of Physics, Durham University, South Road, Durham DH1 3LE, UK*

³ *Department of Physics, University of Surrey, Guildford, GU2 7XH, UK*

Accepted XXX. Received YYY; in original form ZZZ

ABSTRACT

The low dark matter density in the Fornax dwarf galaxy is often interpreted as being due to the presence of a constant density ‘core’, but it could also be explained by the effects of Galactic tides. The latter interpretation has been disfavoured because it is apparently inconsistent with the orbital parameters and star formation history of Fornax. We revisit these arguments with the help of the APOSTLE cosmological hydrodynamics simulations. We show that simulated dwarfs with similar properties to Fornax are able to form stars after infall, so that star formation is not necessarily a good tracer of infall time. We also examine the constraints on the pericentre of Fornax and point out that small pericentres (<50 kpc) are not currently ruled out by the data, allowing for Fornax to be tidally influenced on its current orbit. Furthermore, we find that some dwarfs with large orbital pericentres can be stripped prior to infall due to interactions with more massive galaxies. Tidal effects lead to a reduction in the dark matter density, while the profile remains cuspy. Navarro-Frenk-White profiles are consistent with the kinematic data within 3σ in the innermost regions, while profiles with shallow cusps or cores provide a better fit. We predict that if the reduction of the dark matter density in Fornax occurs, at least in part, because of the action of Galactic tides, then tidal tails should be visible with a surface brightness limit of $\sim 35 - 36$ mag arcsec⁻² over a survey area of ≥ 100 deg².

Key words: cosmology: dark matter – galaxies: dwarf – galaxies: Local Group

1 INTRODUCTION

The Λ CDM cosmological model has been remarkably successful in accounting for the cosmic large-scale structure (Davis et al. 1985; Percival et al. 2001; Tegmark et al. 2004; Springel et al. 2005). On small scales, however, a number of problems persist (Del Popolo & Le Delliou 2017; Weinberg et al. 2015; Bullock & Boylan-Kolchin 2017). In particular, the simplest version of the model predicts that galaxies reside in dark matter haloes that follow a Navarro-Frenk-White profile (NFW), in which the density follows a power law ($\rho \propto r^{-1}$) in the central regions (Navarro et al. 1996b, 1997). This prediction follows from dark matter-only cosmological N -body simulations and has been recently confirmed over 20 orders of magnitude in halo mass (Wang et al. 2019a). On the other hand, measurements of galaxy rotation curves in nearby galaxies (Moore 1994; Flores & Primack 1994; Oh et al. 2008; Kuzio de Naray et al. 2006; Adams et al. 2014; Oh et al. 2015; Zhu et al. 2016a; Read et al. 2017) and some analyses of stellar kinematics in nearby dwarf spheroidals (Battaglia et al. 2008; Walker & Peñarrubia 2011; Amorisco & Evans 2012; Agnello & Evans 2012) appear to favour a ‘core’ in the inner regions, where $\rho \propto r^0$. This has become known as the ‘core-cusp problem’ (de Blok 2010).

One particularly interesting galaxy for the core-cusp problem,

is the Fornax dwarf spheroidal. Fornax is one of the brightest nearby dwarfs and hence large quantities of spectroscopic and photometric data have been collected for this galaxy (Battaglia et al. 2006; Walker et al. 2009; Letarte et al. 2010; del Pino et al. 2015; Kirby et al. 2010, 2013b). These data can be used to place a constraint on its dark matter density distribution. A number of studies using stellar kinematics have favoured a low density core in Fornax (Lokas 2002; Walker & Peñarrubia 2011; Amorisco et al. 2013; Pascale et al. 2018; Jardel & Gebhardt 2012; Read et al. 2019; Sanders & Evans 2020). While several works disagree on whether the data are sufficiently constraining to rule out a central density cusp (Strigari et al. 2006; Richardson & Fairbairn 2013; Genina et al. 2018; Strigari et al. 2018a), all studies to date agree that Fornax has a puzzlingly low inner density as compared to expectations in Λ CDM for a galaxy of Fornax’s stellar mass, by a factor of ~ 3 (Read et al. 2019). Further evidence for a low dark matter density in the central regions of Fornax comes from the survival and present-day positions of its globular clusters. A cored dark matter potential in Fornax permits a wide range of initial conditions for Fornax’s GCs, whereas a cusper potential supports a much narrower range, making it statistically less likely in a Bayesian sense (Goerdt et al. 2006; Cole et al. 2012; Orkney et al. 2019; Leung et al. 2020). However, a cusp cannot be ruled out by such arguments (e.g. Cole et al. 2012; Boldrini et al. 2019; Meadows et al. 2020).

The possibility of a dark matter core in Fornax has encouraged

* E-mail: agenina@mpa-garching.mpg.de (AG)

suggestions for alternative dark matter models (Spergel & Steinhardt 2000; Hui et al. 2017; Lancaster et al. 2020; Elbert et al. 2015; Correa 2020). However, a simpler explanation within the Λ CDM framework is that feedback from supernovae can drive repeated gravitational potential fluctuations that slowly expand dark matter particle orbits, generating a core (Navarro et al. 1996a; Read & Gilmore 2005; Pontzen & Governato 2012; Read et al. 2016; Amorisco et al. 2014). This ‘dark matter heating’ mechanism has been seen in cosmological N -body simulations that attempt to model the multiphase interstellar medium (Mashchenko et al. 2008; Governato et al. 2012; Tollet et al. 2016; Fitts et al. 2017; Oñorbe et al. 2015). Key to exciting this process is to resolve gravitational potential fluctuations driven by gas inflows and outflows. This can happen in simulations where gas is allowed to cool below $T \sim 10^4$ K and reach high density before stars form (Pontzen & Governato 2012; Dutton et al. 2019). However, cores can also form in simulations where gas is not allowed to cool below $T \sim 10^4$ K, provided that the density threshold above which gas can turn into stars is sufficiently high (Benítez-Llambay et al. 2019). Simulations where the threshold is low do not generally produce cores (Sawala et al. 2016; Fattahi et al. 2016a; Bose et al. 2019).

Recent observations, such as in Read et al. (2017, 2019), appear to support the idea that dark matter is ‘heated up’ in at least some dwarf galaxies. Dark matter heating models predict that star formation in dwarfs should be ‘bursty’ (Teysseier et al. 2013), in agreement with data from dwarf populations¹ (Kauffmann 2014; Sparre et al. 2017). Stellar orbits should be heated similarly to the dark matter, which is consistent with the high vertical stellar velocity dispersions observed in dwarfs (Leaman et al. 2012; Teysseier et al. 2013; Hirtenstein et al. 2019). And, these models predict that galaxies whose star formation shut down long ago should be cuspy, which appears to be the case for nearby dwarfs (Read et al. 2019). This latter point is perhaps the best evidence for dark matter heating to date, however, there is an important potential caveat.

The work of Read et al. (2019) used a mixture of nearby dwarf irregular galaxies (dIrrs) and quenched Milky Way spheroidals (dSphs) for their study of dark matter heating, since they required dwarfs with a wide range of star formation histories. While they carefully tested their methodology for both dIrrs and dSphs on a wide array of mock data (Read et al. 2017; Read & Steger 2017; Read et al. 2018; Genina et al. 2020), ideally the dIrrs and dSphs should be treated separately since they have distinct systematics (the former have their dark matter distribution inferred from HI gas rotation curves; the latter from stellar kinematics). The dIrrs in their sample all had sufficient star formation to produce a dark matter core and so they cannot be used on their own to test the idea that galaxies with less star formation should be cuspy. By contrast, almost all of the dSphs in their sample had too little star formation for significant core formation to take place. Only one, Fornax, is both a gas-poor Milky Way satellite and had sufficient star formation to produce a dark matter core, making it a particularly interesting test case.

While Fornax holds the promise of being a rosetta stone for testing dark matter heating models, a concern is its proximity to the Milky Way. This raises the spectre that it could have undergone significant tidal stripping or shocking that act to lower its dark matter

density, potentially mimicking the effect of dark matter heating (Read et al. 2006; Peñarrubia et al. 2009). Read et al. (2019) argue that the recent star formation in Fornax (de Boer et al. 2012), and its typically large pericentre inferred from proper motions (Walker et al. 2008; Gaia Collaboration et al. 2018; Fritz et al. 2018), suggest that Fornax is unlikely to have been subjected to significant tidal effects. Indeed, the observations of the surface brightness profile of Fornax and N -body models of its orbit have so far disfavoured such interpretations (Walker et al. 2006; Battaglia et al. 2015; Wang et al. 2019b). Coleman et al. (2004) hypothesise that the shell structures seen in Fornax could be of tidal origin; however, these structures are relatively young compared to the stellar populations in Fornax, favouring instead a recent merger scenario (Coleman & Da Costa 2005; Coleman et al. 2005, but see also Bate et al. 2015). On the other hand, comparisons with cosmological simulations favour a tidally stripped Fornax (Fattahi et al. 2016a), where the tails are faint, but detectable with current surveys (Wang et al. 2017, 2019b). Simulations in CDM and binding energy arguments also favour an infall time for Fornax of ~ 8 Gyr ago (Rocha et al. 2012; Wang et al. 2016; Fillingham et al. 2019), which suggests that Fornax has spent a long time under the influence of tides. Finally, even if Fornax’s apparent orbit today suggests relative tidal isolation, its orbit and tidal field may have been rather different in the past, especially if it was pre-processed inside an infalling group (Lux et al. 2010).

In this paper, we set out to test whether the inferred dark matter density in Fornax can be reproduced in a Λ CDM cosmological N -body hydrodynamics simulation in which dwarf galaxies do not form cores. In Section 2, we briefly describe our suite of simulations. In Section 3, we identify appropriate analogues of Fornax given its dynamical mass, luminosity, star-formation history and the most recent orbital constraints from *Gaia*. In Section 4, we analyse the formation pathways of the Fornax analogues and compare their inner densities to that inferred for Fornax. In Section 5, we outline the possible limitations of our model for the tidally-induced reduction in the central density of Fornax. In Section 6, we discuss the significance of our results for the core-cusp problem in Fornax. Finally, in Section 7 we present our conclusions.

2 SIMULATIONS

We use the APOSTLE suite of simulations of Local Group-like environments (Fattahi et al. 2016b; Sawala et al. 2016). APOSTLE is based on the EAGLE galaxy formation model and includes models for hydrogen and helium reionization, star formation, gas cooling, metal enrichment, supernovae feedback, AGB winds and AGN (see Crain et al. 2015 and Schaye et al. 2015 for full details). EAGLE is an extension of the P-GADGET-3 code, which itself is an improvement on the publicly available GADGET-2 (Springel 2005). The hydrodynamics are implemented using the pressure-entropy formalism of Hopkins (2013). In APOSTLE, the ‘reference’ EAGLE model is used. APOSTLE assumes a Λ CDM model in the WMAP-7 cosmology (Komatsu et al. 2011). The suite consists of three resolution levels and, in this work, we use the five highest resolution volumes, with dark matter particle masses ranging between $m_{\text{DM}} = 2.5 - 5 \times 10^4 M_{\odot}$ and gravitational softening parameter, $\epsilon = 134$ pc. Gas particles have initial masses in the range $5 - 10 \times 10^3 M_{\odot}$.

Each APOSTLE volume includes two main haloes, which match the Milky Way and Andromeda pair in terms of their total mass, physical separation, relative velocities and the surrounding Hubble flow (Fattahi et al. 2016b). Each of the main haloes hosts a population of dwarf galaxies. The volumes also include nearby iso-

¹ Note, however, that the converse is not true: burstiness does not necessarily imply that a dark matter core must have formed, as demonstrated by the cuspy profiles of dwarf galaxies in the APOSTLE and AURIGA simulations (Bose et al. 2019).

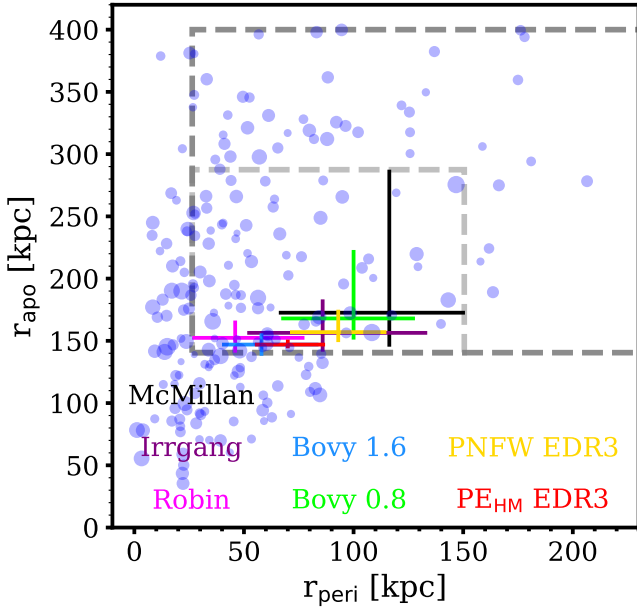


Figure 1. The inferred apocentres and pericentres for all dwarfs within the APOSTLE volumes, which are currently located within 300 kpc of the centre of Milky Way analogues. The area of each point is proportional to the logarithm of the stellar mass at $z = 0$. The labelled error bars mark constraints for Fornax from various potentials described in [Gaia Collaboration et al. \(2018\)](#), [Fritz et al. \(2018\)](#) and [Li et al. \(2021\)](#). The light grey box shows the selection of our sample of Fornax-like orbits and the dark grey box shows a wider selection of dwarfs that have even larger apocentres than those predicted for Fornax.

lated dwarfs. Dwarfs in APOSTLE have been extensively studied in terms of their morphological and dynamical properties ([Campbell et al. 2017](#)), star formation histories ([Digby et al. 2019](#)), metallicities and metallicity gradients (including distinct metallicity subpopulations), and gas content ([Genina et al. 2019](#)). These properties were shown to be consistent, within the resolution limits, with Local Group dwarfs.

In this work, in order to identify bound substructures, we employ the `hbt+` algorithm of [Han et al. \(2018\)](#). `hbt+` makes it particularly straightforward to track haloes across time by assigning each halo a unique ‘TrackID’.

3 METHODS

Our aim is to investigate mass loss in simulated dwarfs similar to Fornax. The simulated Fornax analogues are required to match Fornax according to the following criteria: *i*) an orbit that is compatible with the *Gaia* data; *ii*) halo mass and luminosity; *iii*) star formation history. In the following, we outline the methods behind our sample selection.

3.1 Sample selection

As a first step, we select satellite dwarfs from our simulations, which we define as galaxies that are presently within 300 kpc of either the Milky Way or Andromeda analogues in APOSTLE. Of those, we identify the objects with a stellar mass of at least $10^5 M_{\odot}$, corresponding to stellar populations resolved with ~ 100 particles. We further check that the tidal evolution of these subhaloes is well resolved. Thereafter, we keep all dwarfs which satisfy the criteria in

eqn. 16 of [van den Bosch & Ogiya \(2018\)](#) and have at least 1000 bound dark matter particles at $z = 0$. While the tidal evolution of subhaloes down to ~ 300 particles can, in principle, be resolved according to their eqn. 19, this would still correspond to 0.1 dex scatter in the fractions of bound particles surviving in each of the possible realizations of a dark matter halo. The 1000-particle resolution limit corresponds to dark matter halo masses above a few times $10^7 M_{\odot}$ and leaves us with a sample of 212 resolved luminous dwarfs. As we will show in Section 4.6, the pre-infall halo masses of our sample of Fornax analogues are in the range $4 \times 10^9 - 1 \times 10^{10} M_{\odot}$, corresponding to $\geq 10^5$ dark matter particles at infall. These simulated analogues lose no more than 90 per cent of their maximum mass and are thus robust to the effects of numerical disruption at present day, even for orbital pericentres as small as 10 per cent of the virial radius of the host halo (see fig.10 of [van den Bosch & Ogiya 2018](#), where the yellow band highlights the gravitational softening choice of [Power et al. 2003](#), applicable to our simulations).

3.2 Orbits in the host potential

Next, we approximate the potential of each host galaxy as being spherically symmetric. The potential for a spherically symmetric mass distribution is given by ([Mo et al. 2010](#)):

$$\Phi(r) = -G \int_r^{\infty} dr' \frac{M(< r')}{r'^2}. \quad (1)$$

We compute the potential out to a radius of 400 kpc, where we fix $\Phi(400 \text{ kpc}) = 0$. We thus only consider simulated dwarf galaxies with the maximum apocentre of 400 kpc.

For each dwarf we compute the total energy, E , and the angular momentum, L . Then, for the orbital extremes, where the velocity $\dot{r} = 0$, we have that:

$$\dot{r}^2 = 2[E - \Phi(r)] - \frac{L^2}{r^2} = 0. \quad (2)$$

The solutions of this equation correspond to the apocenter, r_{apo} , and the pericenter, r_{peri} , of the orbit ([Binney & Tremaine 1987](#)). We verify that the approximation of the potential as spherically symmetric is valid in Appendix A.

In Fig. 1, we show the distribution of orbital pericentres and apocentres for all satellite dwarfs with $M_* > 10^5 M_{\odot}$. The error bars of various colours represent constraints for Fornax using three Milky Way models from [Gaia Collaboration et al. 2018](#) (using *Gaia DR2*), two Milky Way models from [Fritz et al. 2018](#) (using *Gaia DR2*) and two models from [Li et al. \(2021\)](#) (using *Gaia EDR3*). The first three are the potentials from [McMillan 2016](#) ($M_{200} = 1.3 \times 10^{12} M_{\odot}$), [Irrgang et al. 2012](#) ($M_{<200 \text{ kpc}} = 1.9 \times 10^{12} M_{\odot}$) and [Robin et al. 2003, 2012](#) ($M_{<100 \text{ kpc}} = 1.2 \times 10^{12} M_{\odot}$). The three potentials differ most significantly in the inner ~ 2 kpc and beyond ~ 40 kpc. *Bovy 1.6* and *Bovy 0.8* are two realizations of the potential from [Bovy \(2015\)](#) with virial masses, M_{200} , of $1.6 \times 10^{12} M_{\odot}$ and $0.8 \times 10^{12} M_{\odot}$, respectively. Finally, we include pericentre and apocentre constraints using *Gaia EDR3* from [Li et al. \(2021\)](#), where a “high-mass” potential from [Retana-Montenegro et al. 2012](#) (PE_{HM}) and a “low-mass” potential from [Pouliasis et al. 2017](#) (PNFW) were used, which are roughly similar in mass to the two models from [Fritz et al. \(2018\)](#). In our sample, we include all orbits contained within the error bars of these models. This is shown as a light grey box in Fig. 1. Additionally, we include dwarfs with larger peri- and apocentres, as we wish to investigate mass loss for these seemingly ‘benign’ orbits. This additional selection is highlighted with a dark grey box in Fig. 1.

3.3 $V_{1/2} - M_V$ relation

Now that the satellite galaxies with orbits similar to Fornax have been identified, we wish to select those which resemble Fornax in their present-day stellar and halo masses. Since neither of these two properties can be measured directly, we use the circular velocity at the deprojected half-light radius of Fornax, $V_{1/2} \approx V_{\text{circ}}(947 \text{ pc})$, and the absolute magnitude in visible light, M_V , as indicative quantities. $V_{\text{circ}}(947 \text{ pc})$ is computed as $\sqrt{\frac{GM(<947 \text{ pc})}{947 \text{ pc}}}$, where 947 pc is 4/3 times the half-light radius of Fornax (710 pc), which is approximately the 3D half-light radius (Wolf et al. 2010) and G the gravitational constant. We obtain the visible magnitudes for our dwarfs using the GALAXEV stellar population synthesis model (Bruzual & Charlot 2003) applied to all bound stellar particles, as determined by the SUBFIND algorithm. Our method is described in more detail in Genina et al. (2019). For comparison with Fornax, we use the corresponding quantities for $V_{1/2} = 20.1_{-1.9}^{+1.9+3.6}$ km s⁻¹ from Fattahi et al. 2016a (where inner errors denote the 25-75th percentiles of the distribution, and the outer errors the 10-90th percentiles) and $M_V = -13.4 \pm 0.3$ from McConnachie (2012).

The values of $V_{\text{circ}}(947 \text{ pc})$ and M_V for our sample of dwarfs are shown in the left panel of Fig. 2, where large colour circles represent the galaxies contained within the dark grey box in Fig. 1, small circles are other satellite galaxies and grey dots are isolated dwarf galaxies. The satellite dwarfs are coloured by $t_{L,90}$, the look-back time at which 90 per cent of their $z = 0$ stellar particles were formed. It can be seen that above the M_V of Fornax, the majority of satellites are still star-forming today.

It is clear from the left panel of Fig. 2 that Fornax is, indeed, somewhat of an outlier in the APOSTLE $V_{\text{circ}}(947 \text{ pc}) - M_V$ relation. Nevertheless, we select a sample of 9 similar galaxies for further inspection. These are marked with different shapes in Fig. 2, which we will continue using in the remainder of this paper. It can be seen that the ‘star’ dwarf is our best Fornax analogue. There is a larger number of isolated dwarfs that match these constraints for Fornax; however, as we shall see below, their star formation histories are incompatible with that of Fornax.

3.4 Star formation histories

We would now like to ensure that our simulated analogues are indeed similar to Fornax in terms of their star formation history (SFH). For our simulated dwarfs, we bin the formation times of all bound stellar particles into the same set of bins as in de Boer et al. (2012). The right panel of Fig. 2 shows the cumulative SFHs of these galaxies as a function of lookback time, normalized by the present-day stellar mass. The solid red line is the median of the 9 simulated Fornax analogues. The blue shaded band is the observational result from de Boer et al. (2012), pink from Weisz et al. (2014) and orange from Rusakov et al. (2021).

Our Fornax analogues, on average, exhibit a similar shape in their SFHs as Fornax. There are two examples that have stopped star formation ~ 6 Gyr ago. This is clearly at odds with Fornax, which, at most, stopped making stars ~ 2 Gyr ago. In the next Section, we will investigate whether this ‘‘quenching time’’ is indicative of the tidal history of this dwarf in our simulations.

The thick grey line on the right panel of Fig. 2 shows the median SFHs of isolated dwarfs. It is clear that these galaxies are still star-forming today and many have an increased star formation rate over the past 5 Gyr. This is incompatible with Fornax whose star formation rate is slowing down around that time. The SFH

of Fornax is certainly more compatible with the simulated dwarfs currently within the virial radius of the Milky Way analogue than with isolated dwarfs.

Now that our sample of dwarf galaxies has been selected we proceed with our analysis and results.

4 RESULTS

4.1 Does the current orbital pericentre reflect tidal history?

It has been argued by Read et al. (2019) that Fornax is unlikely to have undergone significant tidal stripping because it has a relatively large pericentre and is on a nearly circular orbit. These inferred properties, of course, depend on the potential chosen to model the Milky Way. Given the various pericentre values in different potentials from Gaia Collaboration et al. (2018), Fritz et al. (2018) and Li et al. (2021), we examine whether this argument holds in our simulations. We note that the stellar mass, mostly comprised of the disk and bulge, of the Milky Way and Andromeda analogues in APOSTLE is *smaller* by a factor of ~ 2.5 -5 than the stellar mass inferred for the Milky Way (Fattahi et al. 2016b; Sawala et al. 2017), while the virial masses of the haloes, M_{200} , are in the range of values for the Milky Way quoted in the literature (Wang et al. 2020). It is believed that satellite disruption can be enhanced due to interactions with Milky Way’s stellar disk (D’Onghia et al. 2010). This implies that, for a given orbit, on average, the tidal effects are expected to be *less severe* in our simulated potentials than in the Milky Way.

We track each of the APOSTLE satellites back to the time when their dark matter halo mass reached its peak value. In Fig. 3, we show the fraction of bound dark matter mass that has been lost since that time according to the SUBFIND algorithm (left), indicative of tidal stripping, and the dark matter mass lost from within 1 kpc from the centre of each dwarf, indicative of tidal shocks. We note that the mass lost within 1 kpc does not necessarily reflect mass leaving the halo, although this quantity does reflect the reduction in the central density². It can be seen that the vast majority of dwarfs with pericentres below 50 kpc lose more than 80 per cent of their halo mass. Even dwarfs that come only as close as 150 kpc from the centre of the Milky Way lose significant fractions of their mass. Galaxies with large pericentres (> 150 kpc) and less eccentric orbits lose very little mass.

Mass loss from the innermost 1 kpc appears to require more extreme conditions. Galaxies with pericentres < 50 kpc and apocentres < 100 kpc tend to lose more than 80 per cent of their halo mass within 1 kpc. At larger peri- and apocentres the dwarfs typically lose no more than 50 per cent of their mass within 1 kpc. There are, however, some clear exceptions to the trend. In particular, it is interesting that a number of dwarfs with pericentres as large as 100 kpc can still lose large fractions of their innermost dark matter mass.

The shape symbols, as in Fig. 2, show our Fornax analogues. We can see that all of these have pericentres below 100 kpc. Let us look at, for example, the ‘upwards triangle’ Fornax. This galaxy is on a fairly non-eccentric orbit, with a pericentre of ~ 100 kpc, and matches the constraints for Fornax rather well. Nevertheless, it loses ~ 70 per cent of its halo mass and ~ 40 per cent of its mass within 1 kpc. Clearly, even for non-eccentric, large-pericentre orbits, the

² We have verified that a fraction of particles present within 1 kpc at infall is removed completely from the halo, though this is typically a smaller fraction than that displayed on the right of Fig. 3.

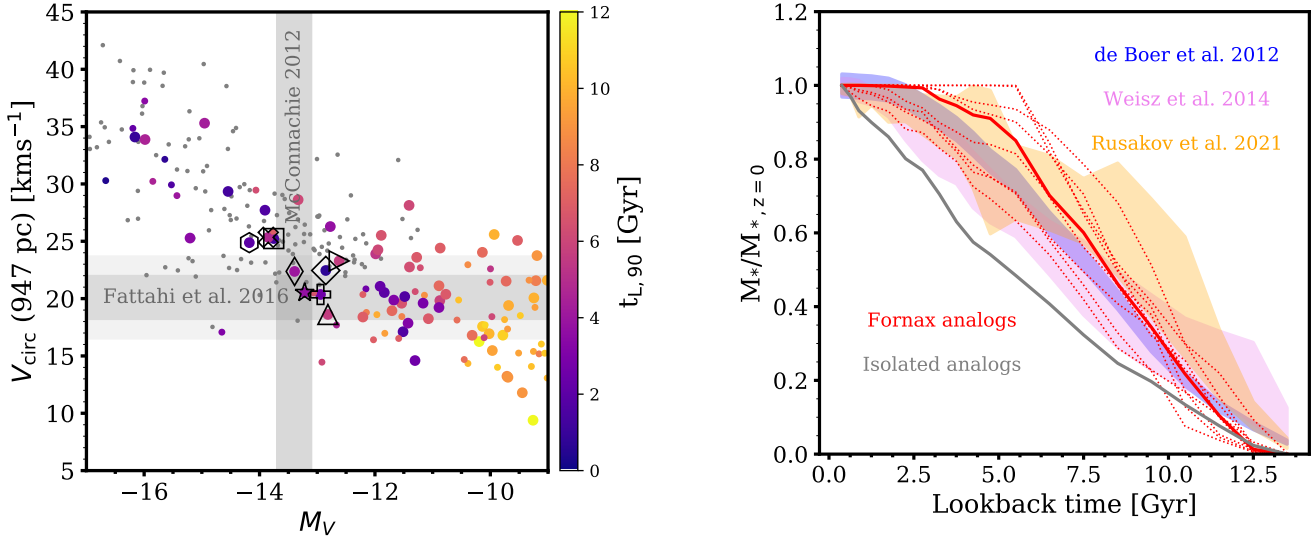


Figure 2. *Left:* the circular velocity at the half-light radius of Fornax, $V_{\text{circ}}(947 \text{ pc})$, as a function of the absolute visible magnitude, M_V . The dark grey and light grey horizontal bands span the 1σ and 2σ errors on the value of $V_{1/2}$ for Fornax from Fattahi et al. 2016a, 2018 ($V_{1/2} = 20.1^{+1.9+3.6}_{-1.9-3.6} \text{ kms}^{-1}$), while the vertical grey band spans the 1σ error on the absolute visible magnitude ($M_V = -13.4 \pm 0.3$) from McConnachie (2012). The thick circles are dwarfs with orbits comparable to Fornax and the thin dots are other satellite dwarfs. The sample of satellites is coloured by the lookback time at which they formed 90 per cent of their $z = 0$ stellar mass, $t_{L,90}$. Symbols of various shapes mark our 9 best Fornax analogues. *Right:* the normalized star formation history of Fornax from de Boer et al. 2012 (blue band), Weisz et al. 2014 (pink band) and Rusakov et al. 2021 (orange band, where we used the upper and lower bands of both Fornax models). The thin red lines show histories for our Fornax analogues and the thick red line is their median. The thick grey line is the median for isolated dwarfs which are similar to Fornax in terms of $V_{\text{circ}}(947 \text{ pc})$ and M_V .

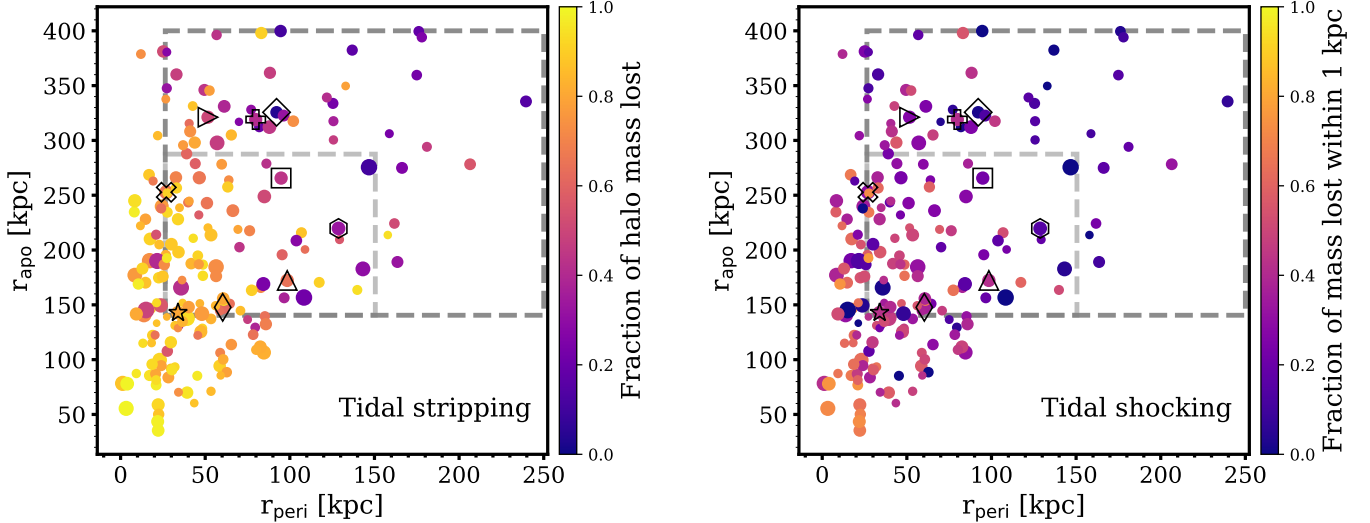


Figure 3. *Left:* the inferred apo- and pericentres of simulated dwarfs, coloured according to the fraction of peak halo mass lost, indicative of tidal stripping. The area of each circle is proportional to the logarithm of the stellar mass at $z = 0$. The grey dashed boxes are as in Fig. 1. The symbols with shapes mark our 9 best Fornax analogues. *Right:* as on the left, but coloured according to the mass lost by each dwarf within the central 1 kpc, indicative of tidal shocks.

galaxies can lose large fractions of dark matter and this phenomenon is not infrequent. Within the light grey box, on the right panel of Fig. 3, 26 per cent of dwarfs lose more than 50 per cent of their dark matter mass within 1 kpc. We will return to the implications of this for the dark matter density of Fornax in Section 4.6.

4.2 Does recent quenching indicate recent infall?

We now consider whether the quenching time is a good indicator of the infall time of a dwarf galaxy and, consequently, an indicator of how much the galaxy has been affected by tides.

On the left panel of Fig. 4 we show the quenching time of each dwarf galaxy, $t_{L,90}$, as a function of its infall time, $t_{L,\text{infall}}$. We define the infall time as the time when the galaxy first crosses the virial radius of a simulated Milky Way analogue. It can be seen that

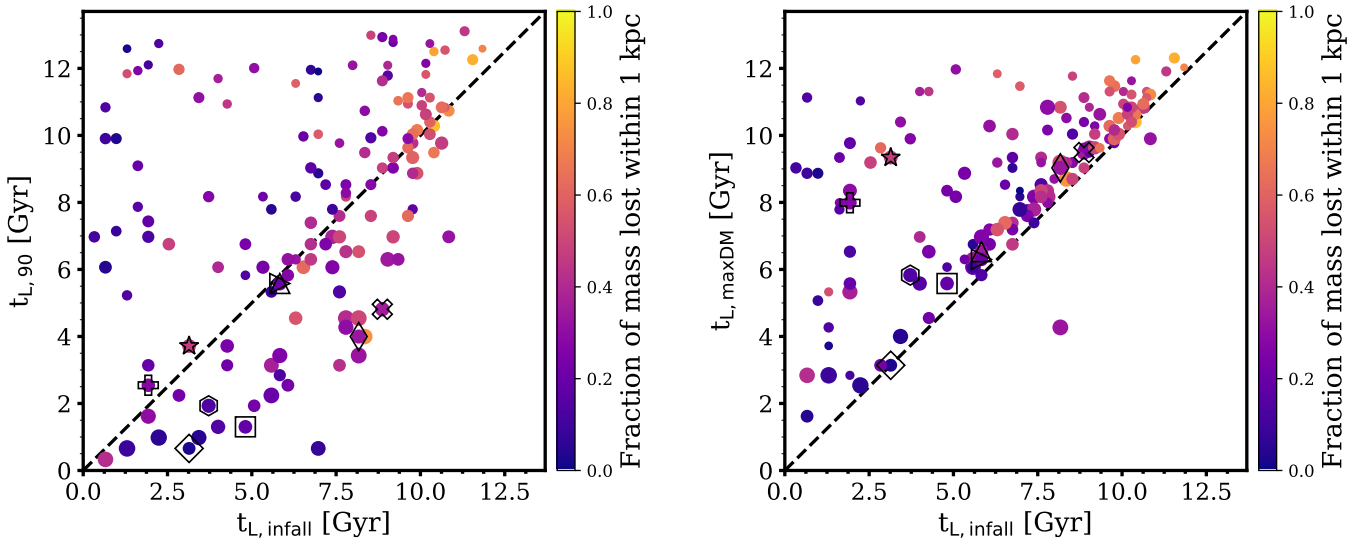


Figure 4. *Left:* the lookback time at which each galaxy forms 90 per cent of its stars, $t_{L,90}$, as a function of the lookback time when it first crosses the virial radius of the host halo, $t_{L,infall}$. The points are coloured by the fraction of mass lost within 1 kpc. The area of the circles represents the logarithm of the $z = 0$ stellar mass. *Right:* the lookback time at which each galaxy had its maximum dark matter halo mass as a function of the infall time, $t_{L,infall}$. The points are coloured by the mass lost within 1 kpc. In both plots the symbols mark the 9 best Fornax analogues and the black dashed lines show the one-to-one relation.

a fraction of simulated dwarfs closely trace a one-to-one relation (black dashed line) between the infall and quenching times (i.e. many satellites are quenched immediately after infall). However, it can also be seen that a number of dwarf galaxies are quenched prior to infall and a number of them after infall.

The area of the points in Fig. 4 is proportional to the logarithm of the present-day stellar mass. It is thus clear that there exists a population of low-mass dwarfs that are quenched prior to infall because of reionization and feedback from star formation (see also Digby et al. 2019). In fact, it can be seen that the smallest galaxies have very early quenching times (~ 12 Gyr) and, as the mass increases, for a given $t_{L,infall}$, quenching is delayed. On the other hand, there exists a population of dwarf galaxies that are generally more massive (closer to Fornax in mass), where quenching occurs after infall (because of ram pressure stripping and tidal stripping of gas inside the host halo). Moreover, as discussed by Genina et al. (2019), a number of dwarfs with large gas supplies are able to form more stars near the pericentre of their orbits³. If gas remains after the first pericentric passage, another star formation burst may occur near the next pericentre. As such, it is clear that, for higher mass objects, the quenching time is not a good indicator of the infall time. Moreover, from the colour of the points (representing the fraction of mass lost within 1 kpc), it can be seen that a number of satellites that are quenched after infall also lose large fractions of their dark matter mass.

On the right of Fig. 4 we show the time at which the galaxy had its maximum dark matter mass, $t_{L,maxDM}$, as a function of infall time, $t_{L,infall}$. In principle, these quantities should have a very similar value. Indeed, we see that for a large number of dwarfs the relation is nearly one-to-one (black dashed line). However, there

also exists a population of galaxies that start losing mass long before infall. Among these objects are some of our best Fornax analogues, including the ‘star’ Fornax, which is a match in both $V_{circ}(947$ pc) and M_V . We also note the presence of the ‘plus’ Fornax in this region, however, as we shall see later, this galaxy simply stops halo assembly ≈ 8 Gyr ago and only experiences minor mass loss through tidal interactions prior to infall. We find that among the population of satellites with orbits compatible with Fornax (light grey box in Fig. 3), nearly 37 per cent have started losing mass more than 2 Gyr prior to infall. From the colours of these galaxies, indicating mass loss within 1 kpc, it is clear that these objects can lose up to $\sim 90 - 99$ per cent of their maximum halo mass, despite very recent infall times in some cases. We conclude that the infall time is not always an adequate indicator of a dwarf’s tidal history.

4.3 The diverse formation histories of Fornax analogues

We now explore the various mechanisms that lead to the formation of our Fornax analogues. These are shown in Fig. 5, where we have selected 9 analogues that are most compatible with Fornax in terms of $V_{circ}(947$ pc) and M_V . In the top subplots, the thick black solid line shows the distance to the host galaxy. The coloured lines show the distances from analogue Fornaxes to simulated dwarfs that at any given point in time were the nearest more massive galaxy. In the bottom subplots, we show the evolution of the dark matter, gas and stellar content. Note that for a number of dwarf galaxies there is a steep rise in mass at early times (~ 11 Gyr). This is likely caused by n_{BT+} incorrectly identifying the main progenitor.

The majority of the dwarf galaxies have very similar formation histories, in which their dark matter haloes are built up early on and dark matter is subsequently lost after infall. Sudden drops in the dark matter content can be seen when the dwarfs approach their pericentres. The majority of our examples follow a very similar history of losing mass due to the effects of tidal stripping from the host galaxy following infall.

The ‘star’ Fornax, our best Fornax match, is indeed a very

³ We point out that the distance–HI relation for APOSTLE dwarfs is in agreement with Local Group dwarfs (see the Appendix of Genina et al. 2019). Additionally, Kelly et al. 2021a and Kelly et al. 2021b find that the hot halo masses of main galaxies in APOSTLE are compatible with those inferred for the Milky Way (Miller & Bregman 2015).

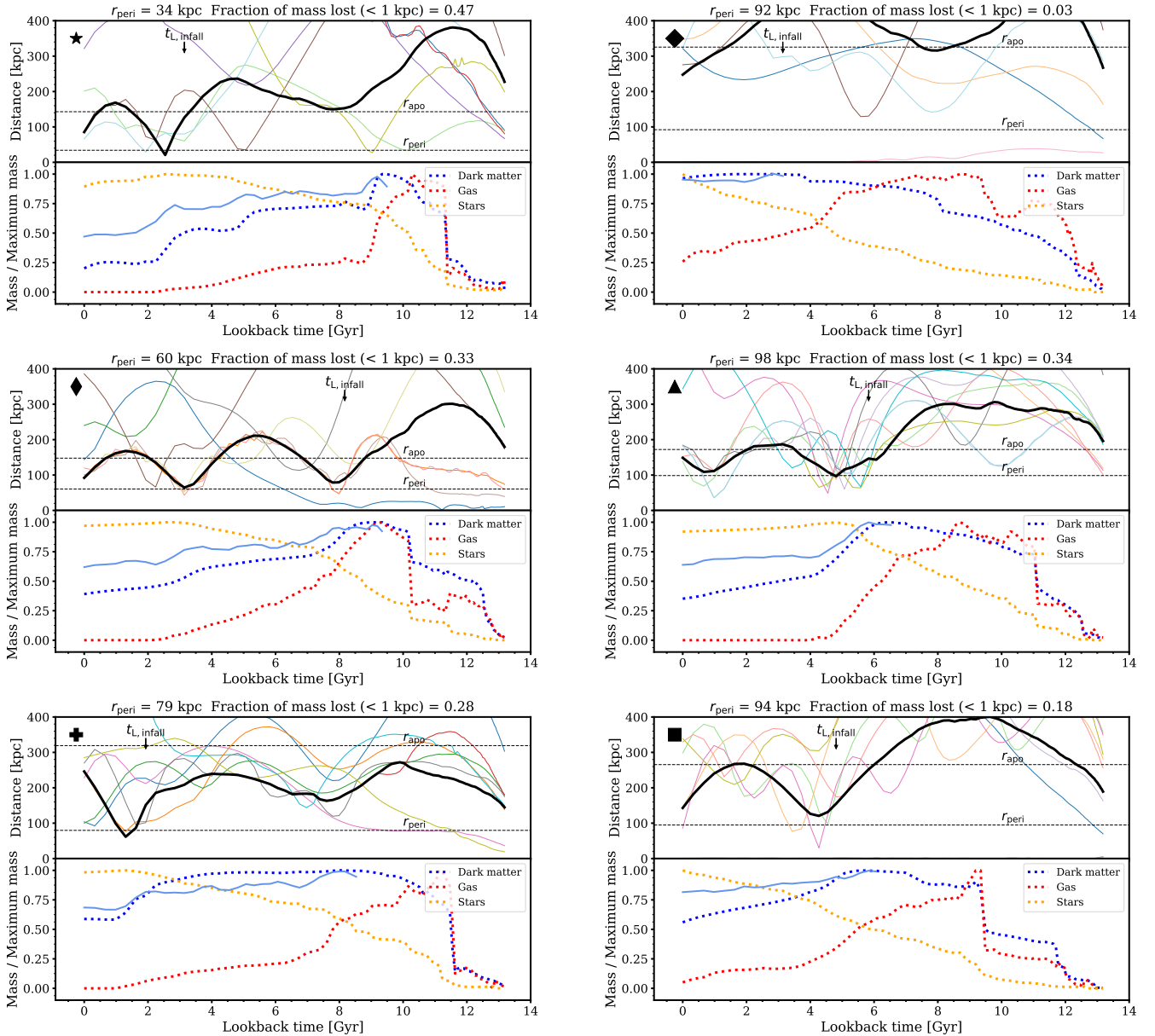


Figure 5. Individual formation and evolutionary histories of the 9 Fornax analogues. Each analogue is marked by the corresponding symbol that we use throughout this work. The top subplots show physical distance to the host galaxy (thick solid line), as a function of lookback time. The inferred peri- and apocentres are shown as thin dashed lines. Lines of different colours show distances to other dwarf galaxies which, at any one point, were the nearest more massive galaxy than the Fornax analogue. The black arrow marks the infall time of each dwarf. The legend shows the inferred value of the orbital pericentre and the fraction of mass lost within 1 kpc. The bottom subplots show the bound dark matter (blue), gas (red) and stellar (yellow) masses, normalized by their historical maximum. The solid light blue line shows the evolution of dark matter mass within 1 kpc from the time the halo had its maximum mass.

peculiar example. Although this galaxy fell in only ~ 4 Gyr ago, it has been losing mass for nearly 9 Gyr. By redshift $z = 0$, the galaxy has lost 80 per cent of the maximum mass it once had and 47 per cent of the mass within 1 kpc. This is because, on two separate occasions, the galaxy interacts with more massive dwarf galaxy fly-bys, each of which strip ~ 25 per cent of its initial mass. While we would expect that the innermost dark matter particles would not be significantly affected in these interactions (Binney & Tremaine 1987), some mass loss within 1 kpc is clearly visible. In this case, while the pericentre is indeed small (34 kpc), it is still not a good indicator of just how much mass the satellites has really lost.

The ‘thin diamond’ Fornax is our second best Fornax analogue. This galaxy loses near 60 per cent of its mass after two pericentres following its infall. The ‘thin diamond’ is an excellent match to Fornax not only in terms of stellar mass and circular velocity but also in terms of quenching time (~ 2 Gyr ago) and its inferred infall time (~ 8 Gyr ago) derived via binding energy arguments (Rocha et al. 2012; Wang et al. 2016; Fillingham et al. 2019). This galaxy, together with the ‘cross’ Fornax, are also clear examples of group infall (the orbits of companion galaxies are shown in blue). While group infall does not seem to play a role in the tidal stripping of these dwarfs, which can be seen to start occurring only after

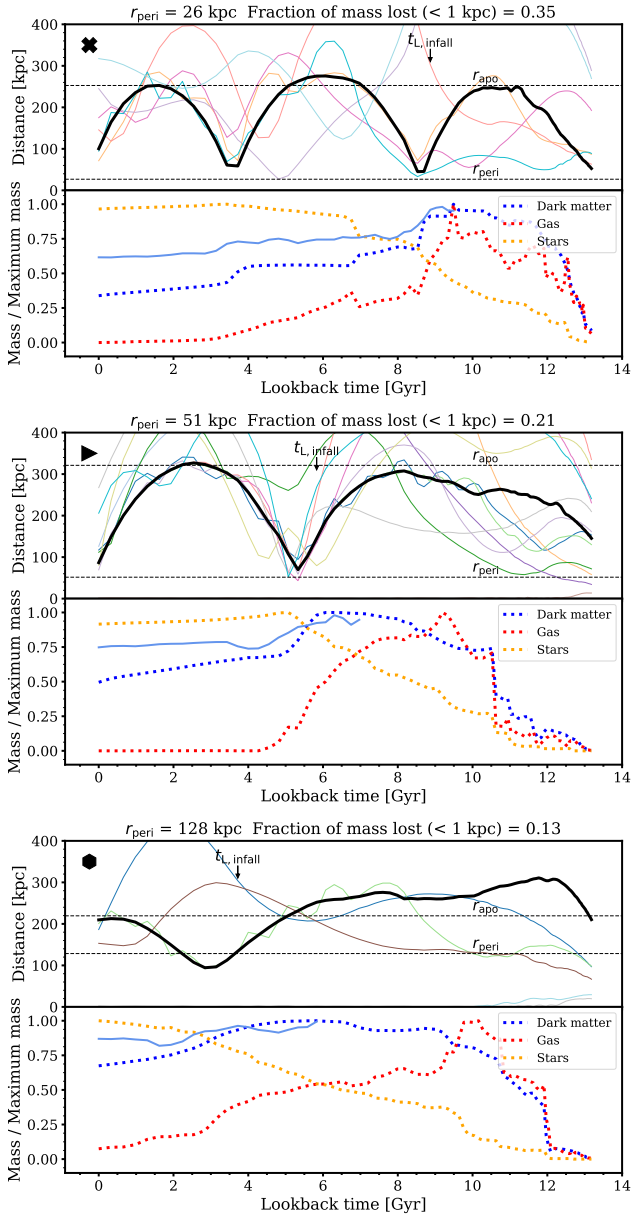


Figure 5 – continued

infall, we note it here as a plausible mechanism of ‘pre-processing’ a satellite galaxy, prior to it crossing the virial radius of the host. Santos-Santos et al. (2021) have shown that LMC-like objects are twice as likely in Local Group-like environments (14 out of 24 host galaxies in APOSTLE have an LMC analogue) than in isolated galaxies. Pre-processed satellites LMC-like objects can ultimately contribute to the dwarf population in the Milky Way.

The ‘thin diamond’ Fornax has a pericentre of ~ 60 kpc, which helps explain the amount of tidal stripping occurring in this dwarf. The value of 60 kpc is well within the error bars for Fornax in a number of Galactic potentials (see Fig. 1). Note, however, the mass loss in the ‘square’ Fornax, which loses nearly 50 per cent of its pre-infall mass and ~ 25 per cent of the mass within 1 kpc. This dwarf has a pericentre of ~ 90 kpc, yet clearly it is able to lose a large fraction of its mass. Note also the ‘upwards triangle’ analogue. The pericentre here is 98 kpc; however, as the satellite falls in ~ 6 Gyr ago, we observe a drop in the dark matter mass by a factor of 2.

Around the same time, we can see that this galaxy is approached by a series of more massive haloes that come as close as 50 kpc to it. This accounts for the enhanced stripping in this dwarf. We see a similar, less severe, occurrence in the ‘right-point triangle’ Fornax (Fig. 5-continued), where the galaxy loses ~ 40 per cent of its initial mass. Also note that at the first pericentre, ~ 5 Gyr ago in these galaxies, there is a burst in star formation. This is an example of one of the mechanisms for the formation of two distinct metallicity populations discussed by Genina et al. (2019).

A complete outlier in terms of formation history is the ‘thick diamond’ Fornax. This galaxy falls in only ~ 3 Gyr ago and has lost less than 10 per cent of its mass. This galaxy had undergone two minor mergers in the last 8 Gyr. This example is slightly fainter than Fornax but has the same value of V_{circ} (947 pc). Evidently, it started off as a very low mass halo that had built up to have a similar V_{circ} (947 pc) to Fornax. Tidal effects are clearly not important for this galaxy.

So far we have seen that, while the processes that lead to the formation of Fornax analogues are quite similar (mass loss at pericentre), $\frac{1}{9}$ of our best Fornax examples have lost some dark matter mass prior to infall, $\frac{2}{9}$ have enhanced mass loss near pericentre by interactions with other dwarfs and $\frac{1}{9}$ came from a low mass halo that was assembled through late minor mergers and never experienced significant mass loss.

4.4 Has the tidal stripping of Fornax been observed?

From our analysis so far, it is clear that in order to match the present-day V_{circ} (947 pc) and M_V of Fornax some tidal stripping is typically required (but not in all cases, as in the ‘thick diamond’ example). Indeed, our best match to Fornax (the ‘star’) has been severely tidally stripped, depleting this galaxy of both the dark matter and the stellar component. The eventful tidal history experienced by this dwarf has left traces in the form of tidal tails, potentially detectable by wide-field photometric surveys. The work of Wang et al. (2019b), using the 3-year data from the Dark Energy Survey (DES), have covered the 25 deg^2 area centred on the Fornax dwarf galaxy. Within this area, down to $32 \text{ mag arcsec}^{-2}$, no tidal features were identified.

We shall now focus on the ‘star’ Fornax, as this galaxy has the most mass in tidal tails of all of our examples. We collect all the stellar particles that have ever been bound to this dwarf and carry out a mock photometric survey. In Fig. 6, we show the surface brightness maps for our ‘star’ Fornax in 25 deg^2 and 400 deg^2 regions. As in Wang et al. (2019b), we use the pixel size of 3 arcminutes. The analogue Fornax is placed at a distance of 138 kpc. We use the small-angle approximation throughout. In order to compensate for the sampling noise in our simulations, we smooth the luminosity in each pixel using a Gaussian filter with a standard deviation of 3 arcminutes. For stellar particles within the tidal tails, however, this is not sufficient to compensate for inadequate stellar sampling. We therefore instead compute the mean surface brightness inside a 7 deg^2 area in the tails (as shown with dashed squares in Fig. 6).

It can be seen that the detection of stars in the tidal streams requires a surface brightness limit of $\sim 35 - 36 \text{ mag arcsec}^{-2}$ (note that in the leftmost two panels of Fig. 6 the stream is denser as it follows a path close to the line-of-sight), which has not been reached with DES (Wang et al. 2019b). Moreover, the area of 25 deg^2 does not seem to provide sufficient coverage to observe the presence of tidal tails, which are clearly visible in the survey area of 400 deg^2 (bottom of Fig. 6). We conclude that a larger spatial coverage and deeper surveys are needed for the detection of tidal tails in Fornax

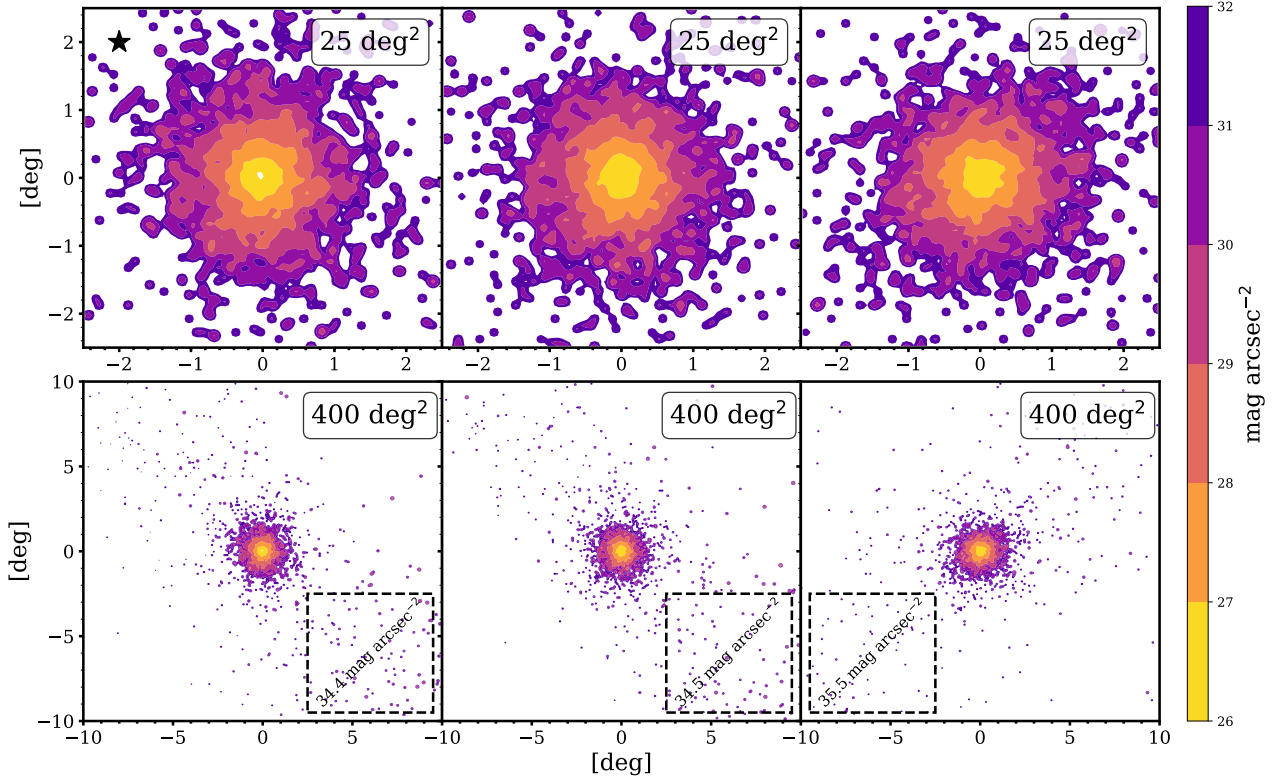


Figure 6. Surface brightness contour maps for our ‘star’ Fornax, for survey areas of 25 deg^2 (as in Wang et al. 2019b) and 400 deg^2 , shown at the top and the bottom, respectively. Each pixel of 0.05 deg^2 has been smoothed using a Gaussian filter with a standard deviation of 0.05 deg . The dwarf is placed at a distance of 138 kpc and projected along the three axes of the simulation cube. The squares select an area of the stellar stream in which we compute a mean surface brightness of stream particles.

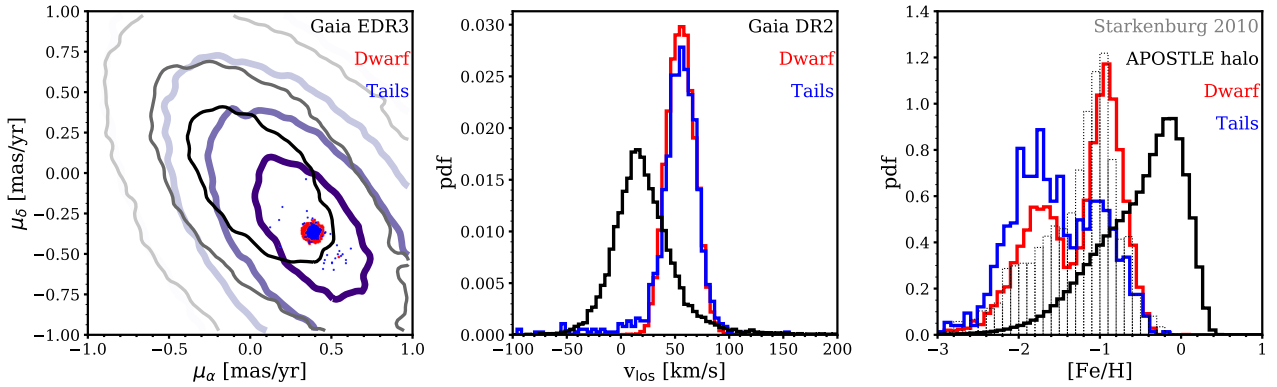


Figure 7. The chemo-kinematic properties of the ‘star’ Fornax analogue. *Left:* The stellar proper motions from *Gaia EDR3* for stars within 1.5 deg of Fornax. The thick contours in shades of purple show regions of equal probability density. Our ‘star’ Fornax analogue is shown with red dots and its tidal tails are shown in blue. The proper motions of the analogue were centred on the Fornax values from Li et al. (2021). The thin grey contours show regions of equal probability density for the stellar proper motions within the “background” region $1.5 < R [\text{deg}] < 10$, centred on Fornax. The contours display the same probability density levels as for the $R < 1.5 \text{ deg}$ region. The contours were smoothed with a Gaussian filter, with the same standard deviation in both cases, for clarity. In the computation of the contours, we include the errors on the proper motions and their correlations. *Middle:* the line-of-sight velocities of the ‘star’ dwarf and of the tidal tails are shown in red and blue, respectively, and are centred on the mean line-of-sight velocity of Fornax (Li et al. 2021). The black histogram shows the distribution of line-of-sight velocities of “background” stars from *Gaia DR2* for the region $1.5 < R [\text{deg}] < 10$, centred on Fornax, with velocity errors included (Gaia Collaboration et al. 2018). *Right:* the metallicity distributions of the ‘star’ dwarf and the tidal tails, as inferred from our simulations, are shown with red and blue histograms, respectively. The dotted histogram shows the metallicity distribution of Fornax from Starkenburg et al. (2010). The black histogram shows the metallicity distribution of the stellar halo of the Milky Way analogue in APOSTLE, computed for the stellar particles located between 8 kpc away from the centre of the host galaxy and the virial radius, R_{200} .

(provided it is stripped as severely as our ‘star’ analogue) and their existence is not presently ruled out.

It should be noted that in our analysis so far we have not considered foreground and background stars, which would significantly complicate the identification of stellar streams. This could in principle be resolved in the future with kinematic and proper motion studies. We explore these prospects further in Fig. 7, where we show the proper motions, line-of-sight velocities and [Fe/H] values⁴ for the stellar particles bound to our simulated dwarf (red), stellar particles in the tidal tails (blue) and the line-of-sight contaminants (black).

In the left panel of Fig. 7 we display the proper motions from *Gaia* EDR3 (Gaia Collaboration et al. 2020) for two regions centred on Fornax: the region within 1.5 degrees of Fornax (purple contours) and the region between 1.5 and 10 degrees from the centre of Fornax (grey contours), corresponding to “background” stars. Note that the latter may indeed include the tidal tails of Fornax. The density contours are computed by sampling a 1000 times, for each *Gaia* source, a multivariate normal distribution defined by the errors on the measurements of the right ascension, μ_α , and declination, μ_δ , proper motions and their correlations. The contours show regions of equal probability density in both samples. The stellar particles belonging to our analogue Fornax are shown in red and its tails are shown in blue. Note that the purple contours are centred on the proper motion measurement of Fornax, where we have artificially placed our ‘star’ analogue.

It is clear that the proper motions of the tails cluster in the same region as the dwarf itself, potentially easing their detection in the future. However, as is clear from the purple probability density ellipses in Fig. 7 (which correspond to stars that are likely to be predominantly Fornax members), the errors on the proper motions are at present large (owing primarily to the relatively large heliocentric distance of Fornax) and it would be difficult to exploit the proper motion measurements to identify the stars belonging to the tidal tails in the near future.

The middle panel of Fig. 7 displays the line-of-sight velocities of the ‘star’ Fornax (red) and its tails (blue), centred on the mean value for Fornax (Li et al. 2021). The black histogram shows the available line-of-sight velocities from *Gaia* DR2 (Gaia Collaboration et al. 2018) for the region between 1.5 and 10 degrees away from the Fornax centre, where we have sampled the errors on each velocity measurement. Again, it is evident that the line-of-sight velocities of the stars in the tails peak at the same value as Fornax itself, potentially easing their identification.

On the right panel of Fig. 7, we display the metallicity distribution of our ‘star’ analogue Fornax in red and its tails in blue. Evidently, there exists a metallicity gradient in this galaxy, resulting in more metal-poor tidal tails. The metallicity distribution of the halo stars in the Milky Way analogue are shown with the black histogram. Here we have included stellar particles between 8 kpc from the centre of the main galaxy and out to the virial radius, excluding the “disk” stars (all stellar particles born bound to the main galaxy) and stellar particles that belong to other satellite dwarfs at $z = 0$. It can be seen that Fornax stellar particles, and the particles in the tails, in particular, peak at much lower metallicities than the halo of the simulated Milky Way analogue. This may, in the future, ease their detection.

It should also be noted that the metallicity distribution of our

‘star’ Fornax analogue has a double-peaked shape (red histogram on the right of Fig. 7), suggesting the presence of two distinct metallicity subpopulations. At least two metallicity subpopulations have also been previously identified in the Fornax dwarf spheroidal (Battaglia et al. 2006; Letarte et al. 2010; Amorisco & Evans 2012). The possible origin of these populations has been discussed in detail in Genina et al. (2019). For comparison, with the dotted grey histogram we show the metallicity distribution for Fornax inferred from spectroscopy (Battaglia et al. 2006; Starkenburg et al. 2010; Lemasle et al. 2014). The two distributions show good agreement; however, we note that the stars outside the half-light radius of Fornax, which would be typically more metal-poor, are likely undersampled. The shape of this metallicity distribution, with a dominant metal-rich peak, is reminiscent of simulated dwarfs which have formed their metal-rich population via a merger. The ‘star’ Fornax has clearly undergone a merger ~ 11 Gyr ago, triggering growth in stellar mass, which is subsequently also enhanced at the time of interactions with other dwarfs (see the yellow dotted line in Fig. 5). The distinct metallicity populations in this Fornax analogue are also spatially segregated, resulting in tidal tails of low metallicity.

4.5 Dark matter density profiles of tidally stripped Fornax analogues

Now that we have established that the majority of our Fornax analogues are able to lose dark matter from the inner 1 kpc due to tidal effects, we wish to compare their dark matter density profiles to the profile inferred for Fornax from its stellar kinematics by Read et al. (2019). Their work used a high-order Jeans analysis method, GRAVSPHERE, to infer the dark matter density distribution in Fornax. The validity of the method has been extensively tested in Read & Steger (2017), Read et al. (2018) and Genina et al. (2020).

In the top left panel of Fig. 8, we show the density profiles of our Fornax analogues at the time they had their maximum dark matter mass (blue) and at the present day (black). It is clear that the inner density has diminished in these galaxies after infall. A number of present-day density profiles appear compatible within the 68–95th per cent confidence levels with the result of Read et al. 2019 (green shaded bands). However, there are two important caveats. Approximately on the scale of $2.8\epsilon \approx 380$ pc (where ϵ is the gravitational softening parameter), the dark matter profiles flatten due to resolution effects (Ludlow et al. 2019). Another important effect is the flattening of the density profiles due to collisional relaxation. A robust prediction for the convergence radius of density profiles comes from Power et al. (2003), who show that NFW profiles are converged at the radius where the collisional relaxation timescale, $t_{\text{relax}} \approx 0.6t_0$, where t_0 is the age of the Universe. This corresponds to approximately 0.6 kpc for our dwarfs.

It is well established that haloes maintain their cuspy shapes in higher-resolution dark-matter-only N -body simulations, although with a larger concentration parameter than their field counterparts (Springel et al. 2008; Navarro et al. 2010; Errani & Peñarrubia 2020). As we are particularly interested in the density in the inner regions, we fit NFW profiles directly to the $z = 0$ density profiles⁵ of our analogues between the Power et al. (2003) convergence radius and the tidal radius⁶. The fitting is carried out using the LMFIT

⁵ We use the *enclosed* densities for the fitting as they are significantly less noisy in simulations than their differential counterparts.

⁶ We define the tidal radius as the radius where the enclosed density of the satellite is equal to the enclosed density of the host up to that radius.

⁴ The metallicities have been computed as in Genina et al. (2019), assuming the solar mass fractions of 0.0014 M_\odot for iron and 0.7381 M_\odot for hydrogen.

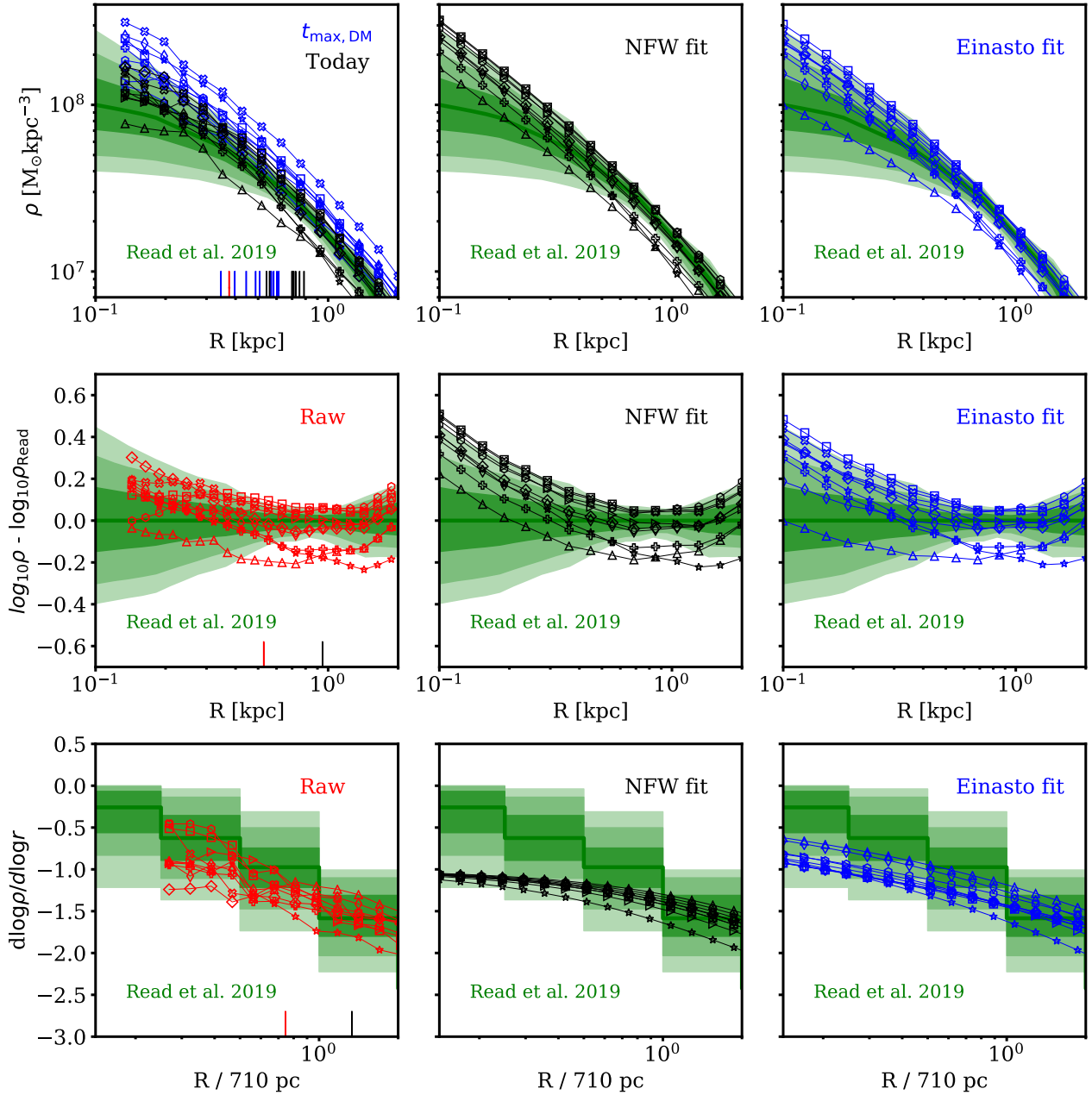


Figure 8. *Top left:* dark matter density profiles of our Fornax analogues, marked with their respective symbols, at the time when they had their maximum dark matter mass (blue) and at the present day (black). The green shaded bands are the 68, 95 and 97.5 confidence intervals for Fornax from [Read et al. \(2019\)](#). The red vertical line marks $2.8\epsilon = 380$ pc. The black and blue vertical lines mark the locations of the [Power et al. \(2003\)](#) radius for each dwarf today and at the time of maximum halo mass, respectively. The left limit on the profiles is set at the gravitational softening $\epsilon = 134$ pc. *Centre left:* logarithmic difference between the $z = 0$ density profiles of our simulated subhaloes and the constraints from [Read et al. \(2019\)](#) (red). The red vertical line marks 2.8ϵ and the black vertical line the mean location of the [Power et al. \(2003\)](#) radius. *Bottom left:* the log-slope of the density for our Fornax analogues, compared to the log-slope constraints for Fornax from [Read et al. \(2019\)](#). The values are shown at fixed fractions of the half-light radius of Fornax (710 pc). The red and black vertical lines mark 2.8ϵ and the mean [Power et al. \(2003\)](#) radius, respectively. *Middle column:* the best NFW profile fits to our Fornax analogues at $z = 0$ (top); the logarithmic difference from the results of [Read et al. 2019](#) (middle) and the log-slope of the profile (bottom). *Right column:* the same as the middle column, but for the best Einasto profile fits. Einasto shape parameters are in the range 2.96 - 4.54.

algorithm ([Newville et al. 2016](#)), minimizing the χ^2 function in 21

log-density bins, as defined in [Neto et al. \(2007\)](#). The NFW profile is defined as

$$\rho(r) = \frac{\rho_s}{\frac{r}{r_s} \left(1 + \frac{r}{r_s}\right)^2}. \quad (3)$$

We find the scale density, ρ_s , and the scale radius, r_s , that minimize χ^2 . The resulting profiles are shown in the top-centre panel of Fig. 8, while the middle-centre panel shows the logarithmic difference of the fitted NFW profiles from the profiles inferred by Read et al. (2019). It is clear that our Fornax analogues are typically denser in the centre than Read et al. (2019) predict. Only three analogues are consistent with Read et al. (2019) within 99.7 per cent confidence in the region 0.1-2 kpc. At 150 pc, 6 of the analogues have densities consistent with Fornax within the 99.7 per cent confidence interval and 3 within the 95 per cent confidence interval.

So far we have only compared the absolute magnitudes of the density at each radius. In order to compare the *shapes* of the profiles more effectively, we display the log-slope of the density in the bottom row of Fig. 8. The red lines show the slopes obtained directly from the simulations and the black lines the slopes of the fitted NFW profiles at each radius. The green bands show the results of the kinematic analysis of Read et al. (2019). Note that Read et al. (2019) use a broken power-law fit to the density profiles, where the breaks occur at fixed intervals of the half-light radius $[0, 0.25, 0.5, 1, 2, 4]R_e$. It can be seen that raw simulation profiles with shallow cusps on the scale of the gravitational softening (red vertical line in Fig. 9), are typically consistent with the result of Read et al. (2019)⁷ within the 95 per cent confidence level at all radii, while the NFW profiles are consistent within the 97.5 per cent confidence level in the central regions and within 95 per cent near the half-light radius.

We additionally consider the Einasto functional form (Navarro et al. 2010) for the simulated Fornax analogues,

$$\rho(r) = \rho_{-2} \exp \left[-2\alpha \left(\left(\frac{r}{r_{-2}} \right)^{\frac{1}{\alpha}} - 1 \right) \right], \quad (4)$$

with ρ_{-2} being the density at the radius r_{-2} , where the log-slope of the density profile is -2. The parameter, α , is the Einasto shape parameter. Again, we find a set of parameters ($\rho_{-2}, r_{-2}, \alpha$) that minimize χ^2 . We find Einasto shape parameters in the range 2.96 - 4.54, consistent with the range found in Di Cintio et al. (2013) for cuspy subhaloes in the DMO and SPH versions of the CLUES simulations.

The results of the fit are shown in the right column of Fig. 8. Einasto profiles allow for inner density cusps that are shallower than NFW. With this parameterization, we find that 5 of the Fornax analogues are consistent with the limits of Read et al. (2019) within the 97.5 per cent confidence interval in the radial range 0.1-2 kpc. At 150 pc, 8 of the analogues have densities consistent with Fornax within the 97.5 per cent confidence level and 4 within the 95 per cent confidence level. In terms of the log-slope of the density (bottom right panel of Fig. 8), 2 of the analogues are consistent with Fornax across the radial range 0.1-2 kpc and, as in the NFW case, all profile shapes are consistent with Fornax within the 97.5 per cent confidence levels.

It is clear from Fig. 8 that central dark matter densities compatible with Fornax can be obtained through the effects of tidal stripping; however, based on our extrapolation, the shapes of the corrected density profiles of stripped NFW haloes appear to be less

similar to that of Fornax than those of haloes with a shallow cusp or a small core in the central regions. However, we also note that the relatively small mass of stellar disks in APOSTLE host galaxies suggests that the strength of tidal effects is underestimated in these simulations, particularly for small-pericentre orbits. In the left panel of Fig. 2, the enhanced stripping would result in lower values of V_{circ} , accompanied by little change in M_V . This could place the central densities of simulated analogues in better agreement with Read et al. (2019).

4.6 The tidally induced reduction in the central densities of Fornax analogues

We now explore how the dwarf galaxies in our sample compare to Fornax in the context of the central density - virial mass ($\rho_{150} - M_{200}$) relation (see the middle panel of fig. 5 in Read et al. 2019). To obtain the ρ_{150} values, we fit NFW profiles to the subhaloes in our simulations at $z = 0$, as described in Section 4.5. The estimated densities at 150 pc are shown as red circles in the left panel of Fig. 9. We also show the densities of these subhaloes at the time of maximum R_{max} , where R_{max} is the radius where the circular velocity profile peaks⁸. The time of maximum R_{max} corresponds approximately to the infall time of a subhalo. In certain cases, an NFW profile provides a poor fit⁹ to the subhaloes at $z = 0$. For these subhaloes, we apply the tidal tracks of Errani & Navarro (2020) (using their equations 7 and 9) to the fitted profile at the time of maximum R_{max} to deduce the value of ρ_{150} at $z = 0$. These values are shown with red squares, while the black squares are the ρ_{150} values at the time of maximum R_{max} , obtained through fitting NFW profiles. In the bottom subplot of Fig. 9 we compare these estimated values to the ones obtained from NFW profile fits for cases where such a fit is possible. It can be seen that these estimates are effectively unbiased at all halo masses. We further discuss the Errani & Navarro (2020) tracks and their applicability to our simulations in Appendix B.

The black and red symbols of different shapes represent our Fornax analogues. The grey shaded band is taken from the mass-concentration relation of Dutton & Macciò (2014) and the blue band is the densities expected for dwarfs with the same masses and concentrations that have undergone complete core formation below the half-light radius (the corresponding density profile is described in Read et al. 2016). The green point with error bars is the inferred density of Fornax at 150 pc from Read et al. (2019), while the pink point shows the value inferred by Hayashi et al. (2020) using axisymmetric Jeans analysis. In this figure, we notice two interesting features:

Firstly, the pre-infall M_{200} for our sample of Fornax analogues is systematically lower than that inferred by Read & Erkal (2019). We predict a pre-infall $M_{200} \approx 4 - 9 \times 10^9 M_{\odot}$ for Fornax. The origin of this discrepancy is not straightforward and we will discuss this point further in Section. 5.2. The dotted red and blue lines show the 1σ span of the present-day masses of Fornax inferred by Errani et al. (2018) for cuspy and cored haloes, respectively. As the horizontal axis of Fig. 9 displays the pre-infall halo mass, we show the present-day bound mass for our Fornax analogues with

⁷ We note that the broken-power-law model for the density distribution in GRAVSPHERE, together with the requirement that the density should decrease outwards, generally disfavours density distributions with cores $> 0.25R_e$ (Read et al. 2019). We have checked, however, that the CORENFWTIDES model, where such cores are allowed, still permits NFW-like cusps in the central regions of Fornax within the 95 per cent confidence levels.

⁸ For pre-infall haloes, we fit the NFW profile in the radial range between the Power et al. (2003) convergence radius and R_{200} in 31 logarithmic bins.

⁹ Here we define the goodness of fit as the fitted profile being within 15 per cent of the raw profile across the entire fitted radial range.

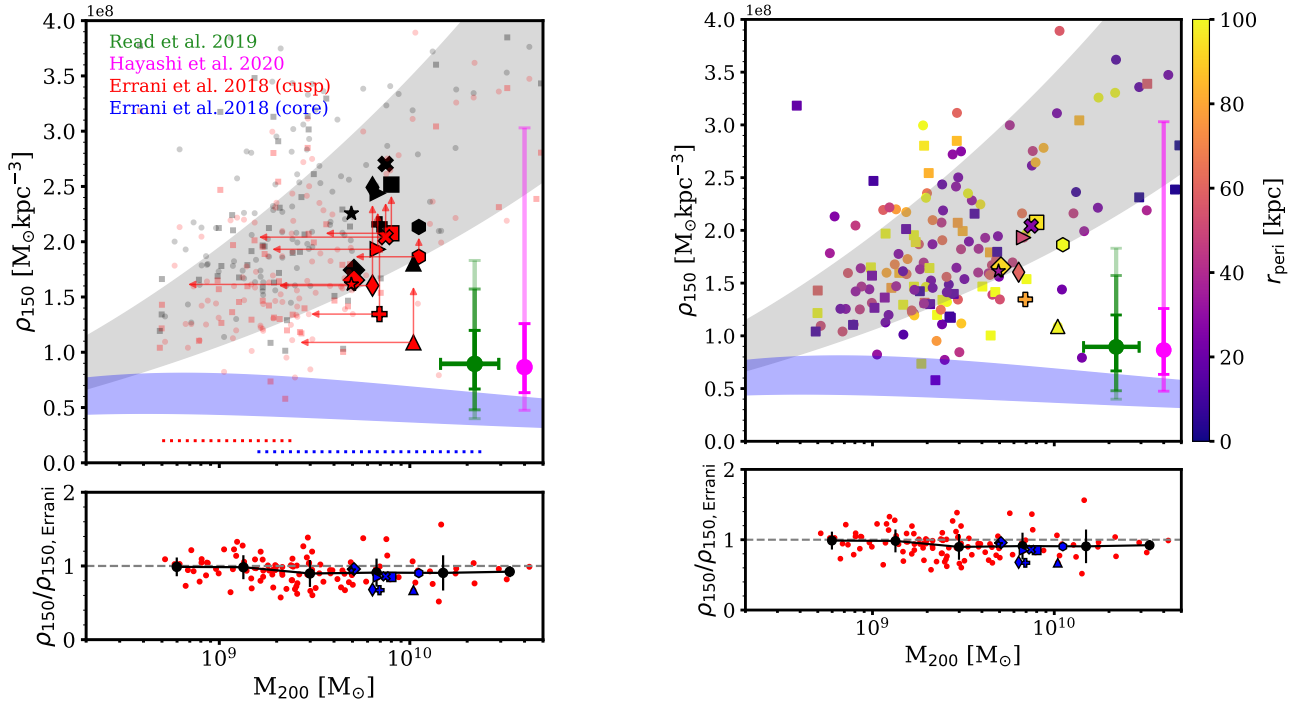


Figure 9. *Left:* the density at 150 pc, ρ_{150} , as a function of all-time maximum virial mass, M_{200} , of each dwarf satellite. The black symbols show the densities at the time of maximum mass within R_{\max} and the red symbols the densities at the present day. Circles show the densities inferred from a direct NFW profile fit, while squares show densities inferred from application of the Errani & Navarro (2020) tidal tracks to the NFW profile fits at the time of maximum mass within R_{\max} . The green point and error bars display the median and 68-95-97.5 confidence intervals of ρ_{150} for Fornax from Read et al. (2019); the point is positioned at the pre-infall halo mass value derived by Read & Erkal (2019). The pink errorbar shows the 68 and 95 per cent confidence intervals of ρ_{150} for Fornax, derived by Hayashi et al. (2020). The pink point is offset to the right of the green one for clarity. The dotted red and blue horizontal lines show the 1σ span of the total present-day mass of Fornax for a cuspy (red) and cored (blue) halo, derived by Errani et al. (2018). The grey shaded region is derived from the mass-concentration relation of Dutton & Macciò (2014) and the blue shaded band is the equivalent relation for CDM haloes that form a core below the half-light radius. The various symbols mark our 9 Fornax analogues. Each of these have ρ_{150} values derived by fitting an NFW profile. The red upwards-pointing arrows show their ρ_{150} values derived using the Errani & Navarro (2020) tracks. The left-pointing arrows show the total bound mass at $z = 0$. The bottom panel shows the comparison between the $z = 0$ values of ρ_{150} derived from an NFW profile fit (where the fit was possible) and the densities derived from the method of Errani & Navarro 2020 (red dots). Blue symbols are our Fornax analogues. The two estimates are consistent with each other for $M_{200} < 3 \times 10^{10} M_{\odot}$ within 1σ , though there is a systematic bias for $M_{200} > 10^9 M_{\odot}$ of ~ 10 per cent. *Right:* the values of the present-day ρ_{150} and all-time maximum, M_{200} , coloured by their inferred orbital pericentres of each dwarf satellite. Different symbols highlight our Fornax analogues.

left-pointing arrows. Five of the analogues are consistent with the value inferred by Errani et al. (2018) within 1σ .

Secondly, there is a large number of dwarf satellites, including several of our dwarf analogues, whose ρ_{150} is consistent with that of Fornax (Read et al. 2019), purely due to tidal effects. It can be seen that tidal effects in our simulations are able to reduce the central density of satellite dwarfs by a factor of 2-3. We also note that all of the analogues are consistent with the ρ_{150} value inferred by Hayashi et al. (2020) within 2σ .

An important aspect of the argument presented by Read et al. (2019) is that the classical dwarfs shown in their fig. 5, including Fornax, are unlikely to have undergone significant tidal stripping and shocking based on their orbits as inferred from *Gaia* data. Thus, the low density in Fornax is interpreted as being due to core formation rather than tides. In the right panel of Fig. 9, we show the present-day densities of dwarfs as a function of M_{200} , coloured by their inferred pericentres. We emphasize that these pericentres are derived using a directly measured spherically symmetric host halo potential from the simulations.

The majority of dwarfs with particularly low central densities do indeed have low pericentres; yet there are a number of outliers.

Most notably, our ‘upwards triangle’ Fornax, with a pericentre of 98 kpc, has a density comparable to that of Fornax. We do, however, note that, unlike Fornax, this galaxy was quenched ~ 5 Gyr ago. The ‘plus’ Fornax analogue is another example with a pericentre of 79 kpc and a central density compatible with that of Fornax. This galaxy was only quenched ~ 2 Gyr ago. Its halo mass, however, places it in a position, where it is fully compatible with Λ CDM. We note again that a number of Milky Way potentials in the literature predict pericentres for Fornax as low as 20-30 kpc.

5 HOW LIKELY IS THE TIDAL ORIGIN OF THE LOW DARK MATTER DENSITY IN FORNAX?

We have so far shown that in Λ CDM simulations in which baryonic feedback *does not* cause core formation, ‘core-like’ densities may be encountered in Fornax-like haloes with eventful tidal histories which are not always reflected in their inferred orbital pericentres. There are four main possible sources of tension between our results and previous works: *i)* high central densities observed for dwarf galaxies with smaller pericentres than Fornax (Kaplinghat et al.

2019); *ii*) the value of the pre-infall mass, M_{200} , of Fornax; *iii*) the assumed pericentre of Fornax; *iv*) possible numerical effects. We discuss these below.

5.1 Comparison with the density-pericentre anticorrelation

A possible discrepancy with our results is presented by [Kaplinghat et al. \(2019\)](#) who have shown that the central densities of a sample of 9 bright Milky Way satellites appear to increase with decreasing orbital pericentre. It therefore seems paradoxical that Fornax, with its relatively large orbital pericentre, should have its density significantly reduced by tides, while other dwarfs, with smaller inferred pericentres, do not.

Firstly, we emphasise that for our best Fornax analogue much of the stripping occurs *prior to infall* into the host galaxy. In another example (the galaxy indicated by an ‘upward triangle’ in some of the figures), the pericentre is, in fact, ~ 100 kpc, but stripping is enhanced by encounters with other massive objects. Secondly, as we have pointed out in [Fig. 1](#), the pericentre of Fornax is dependent on the assumed Milky Way potential. Note that this is not the case for many other classical dwarfs ([Borukhovetskaya et al. 2021](#)), mainly affecting those at large Galactocentric distances (Leo I, Leo II, Canes Venatici I).

We now aim to establish whether a density-pericentre anticorrelation exists in our simulations. In CDM, this may occur because of tidal effects, whereby subhaloes with small pericentres are disrupted and those with large pericentres survive. This ‘survivor bias’ would then lead to an anticorrelation in the density-pericentre plane ([Kaplinghat et al. 2019](#)). In the left panel of [Fig. 10](#) we show the densities at 150 pc of all satellites in APOSTLE (those with and those without stars) as a function of pericentre. We derive the values of ρ_{150} by directly fitting an NFW profile to the subhaloes at the time of their maximum R_{\max} and applying the method of [Errani & Navarro \(2020\)](#) to estimate ρ_{150} at the present day. As we have shown in [Fig. 9](#), this method is an unbiased estimate of the densities we would have obtained by a direct NFW profile fit.

We show the densities estimated by [Kaplinghat et al. \(2019\)](#) for a sample of classical dwarfs with yellow circles on the left of [Fig. 10](#) and for the ultra-faint dwarf sample in purple. We also show the densities estimated for the same sample of classical dwarfs (excluding Canes Venatici I) by [Hayashi et al. \(2020\)](#) with blue circles. In all cases, we assume the *PNFW* Milky Way potential with *Gaia* *EDR3* data ([Li et al. 2021](#)).

The satellites in [Fig. 10](#) are coloured by their value of V_{peak} . Firstly, we see that dwarfs that are denser at the present day have, unsurprisingly, larger values of V_{peak} . Secondly, we observe a trend whereby starting from a pericentre of ~ 100 kpc and below, the number of surviving subhaloes decreases for smaller V_{peak} . This is similar to the ‘survivor bias’ also seen in the dark-matter-only simulations presented by [Hayashi et al. \(2020\)](#). Some dwarfs with smaller V_{peak} clearly still exist and have small pericentres. However, we have verified that many of these are recently accreted objects. Finally, at very small pericentres (< 20 kpc), a cluster of points can be identified, where the densities seem to decrease with pericentre. This is indicative of dwarfs that are currently in the process of tidal disruption.

In order to quantify the density-pericentre relation in our simulations, we repeat the procedure of [Kaplinghat et al. \(2019\)](#), now fitting a power law to the full population of subhaloes of each Milky Way analogue. The distributions of best-fit slopes are shown with a black histogram in right-upper panel of [Fig. 10](#), where the bands bracket the results for all satellite populations. The distribution of

best-fit slopes for the classical dwarfs using the density estimates of [Kaplinghat et al. \(2019\)](#) is shown as a yellow histogram and the distribution obtained using the density estimates of [Hayashi et al. \(2020\)](#) is shown as the blue histogram. From the right-bottom panel of [Fig. 10](#) it can be seen that these two distributions are statistically consistent with APOSTLE, within 1σ for the [Hayashi et al. \(2020\)](#) sample and 2σ for the [Kaplinghat et al. \(2019\)](#) sample, although a shallower anti-correlation is preferred in our simulations. Applying the same fitting procedure to all satellites hosting at least one stellar particle, we obtain the grey histogram in the bottom panel of [Fig. 10](#). This, in general, suggests no correlation for the sample of luminous satellites, although the distribution appears somewhat double-peaked, where some analogues tend to a weak negative correlation and some to a weak positive correlation. We must bear in mind, however, that these objects are a biased subset of the broader distribution with a generally negative trend (which includes ultra-faint dwarfs whose stellar populations are unresolved).

The purple histogram in [Fig. 10](#) shows the distribution of inferred power-law slopes for the sample of ultra-faints from [Kaplinghat et al. \(2019\)](#). This generally prefers much steeper slopes than the classical dwarfs. One can also see a second peak in this distribution, at a positive power-law slope of 1.5. We show that this is primarily due to the inclusion of Crater II in this sample – a clear outlier in terms of its density. It may seem surprising that this dwarf should affect the inferred power-law slope to such an extent; however, this dwarf has the smallest error bars on the density of the entire sample of ultra-faints, giving this data point greater weight. If this dwarf is removed from the sample, the inferred power-law slope for the ultra-faints becomes consistent within 1σ with the classical dwarfs (pink histogram).

Although the distributions of the best-fit power-law slopes in the observations and simulations are consistent within 1 or 2σ , it is nonetheless clear that the data (both for the ultra-faints and the classical dwarfs) prefer steeper power-law slopes and, for the [Kaplinghat et al. \(2019\)](#) sample, the scatter is narrower than in our simulations. There are two points to consider here: *i*) the strength of the Milky Way potential and *ii*) the sample of observational data.

On the first point, we must note that the stellar disks of the host galaxies in the highest-resolution APOSTLE simulations have relatively low masses. The stellar mass is $\sim 1 - 2 \times 10^{10} M_{\odot}$ ([Fattahi et al. 2016b](#)), compared to the estimated $5 \times 10^{10} M_{\odot}$ for the Milky Way ([Licquia & Newman 2015](#)). Comparing APOSTLE with the AURIGA ([Grand et al. 2017](#)) simulations ($M_{*} \sim 1 - 7 \times 10^{10} M_{\odot}$), [Richings et al. \(2020\)](#) have shown that only ~ 30 per cent of subhaloes in AURIGA with halo mass $M_{\text{DM}} > 10^8 M_{\odot}$ survive at a radius of 10-20 kpc (compared to dark-matter-only simulations), while in APOSTLE ~ 50 per cent of the substructures survive. This is due to the stellar masses of the central galaxies in AURIGA being twice as large as those in APOSTLE. The Milky Way analogues in APOSTLE typically have lower stellar masses than the estimates for our Galaxy ([Fattahi et al. 2016b](#)), while the stellar masses in AURIGA are typically higher. We thus expect that the gradient representing surviving subhaloes in the density-pericentre plane would steepen in simulations where the mass of the stellar disk is higher.

On the second point, our simulated samples clearly include objects that are currently in the process of tidal disruption, the dwarf irregulars and the recently accreted objects. The sample of [Kaplinghat et al. \(2019\)](#), on the other hand, excludes Sagittarius dSph (with a pericentre of 15 kpc and likely a lower dark matter density than expected from the anti-correlation relation at this pericentric distance), as well as the Large and Small Magellanic Clouds ([Lokas et al. 2010](#); [Vasiliev & Belokurov 2020](#)). The ultra-faint sample

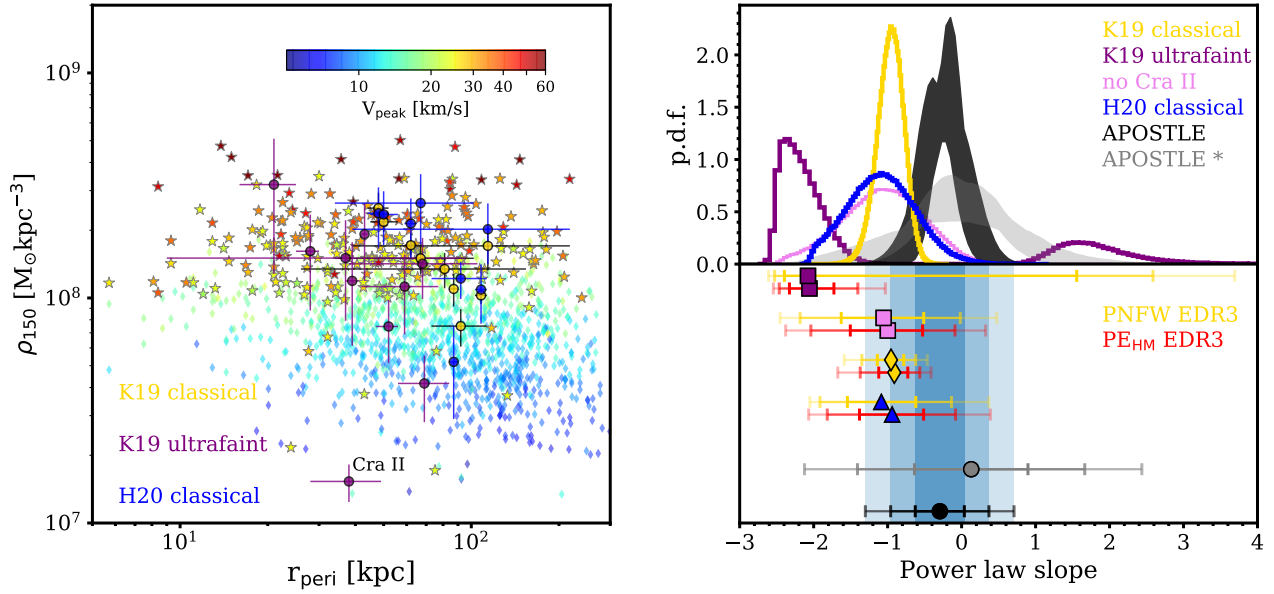


Figure 10. *Left:* the density at 150 pc as a function of pericentric distance, for the entire population of resolved satellites in APOSTLE. Satellites hosting at least one stellar particle are identified with ‘star’ symbols and dark satellites with ‘diamonds’. The symbols are coloured by their historical maximum circular velocity, V_{peak} . Haloes with $V_{\text{peak}} \geq 19$ km/s form stars. Circles with error bars show the densities at 150 pc inferred by Kaplinghat et al. (2019) for 9 of the Milky Way’s classical dwarfs, with pericentres taken for the PNFW Milky Way potential using Gaia EDR3 (Li et al. 2021). Blue circles are density estimates for the same dwarfs (apart from Canes Venatici I) by Hayashi et al. (2020). The purple circles show the densities of the sample of ultra-faint dwarfs from Kaplinghat et al. (2019). *Top right:* the distribution of best-fit power-law slopes for the Kaplinghat et al. (2019) sample of classical dwarfs (yellow), the Kaplinghat et al. (2019) sample of ultra-faints (purple), ultrafaints excluding Crater II (pink), and for the Hayashi et al. (2020) sample of classical dwarfs (blue). The entire sample of satellites for each Milky Way analogue in APOSTLE is shown in black, where the bands bracket the distributions. The APOSTLE satellites of each analogue which host at least one stellar particle are shown in grey. *Bottom right:* median (symbols) and 68, 95 and 97.5 confidence intervals (error bars) for the power slopes, computed for each sample of dwarfs in the PNFW (yellow) and the PE_{HM} (red) potentials (Li et al. 2021). For APOSTLE, we show the mean of the power-law slope distributions for the entire sample of satellites (black) and for the sample of luminous satellites (grey). The blue bands highlight the 68, 95 and 97.5 confidence intervals of the mean power-law slope for all satellites in different Milky Way analogue potentials.

excludes dwarfs which likely fell in as part of a group (Patel et al. 2020), dwarfs where the sample of kinematic tracers is too small and dwarfs for which the measured velocity dispersion is too low to be inconsistent with no velocity dispersion (for example, Triangulum II and Segue II (Kirby et al. 2017, 2013a), both of which are very underdense galaxies with small inferred pericentres Li et al. 2021).

Moreover, if one considers instead the central densities inferred for the classical dwarfs by Hayashi et al. 2020 (shown with blue points in Fig. 10), using axisymmetric Jeans modelling (we note again that many of the classical dwarfs are known to be aspherical), a density-pericentre trend is no longer obvious and the power-law fit to these data is not necessarily justified. As the models of Hayashi et al. (2020) are more permissive of different tracer distributions in 3D, the density error bars increase and several of the classical dwarfs have densities offset from those of Kaplinghat et al. (2019) by more than 1σ . This suggests that the error bars of Kaplinghat et al. (2019) lack a systematic error contribution due to the asphericity of the stellar and halo components. Additionally, as we have shown in this work, the inferred pericentres are dependent on the chosen Milky Way potential, such that the error bars on the pericentre are likely underestimated, particularly for the more distant dwarfs.

The sample of ultra-faint dwarf galaxies (purple points in Fig. 10) appears to follow a different trend to the classical dwarfs. Kaplinghat et al. (2019) have estimated their central densities using the Wolf et al. (2010) mass estimator; the error bars, however, are large because of the small stellar samples for these objects and

because a range of NFW parameters is able to reproduce the mass within the half-light radius. If the derived relation for the classical dwarfs also describes the ultra-faints, this would imply that in many ultra-faint dwarfs the Wolf et al. (2010) estimator is biased low by several σ and, in some cases, by orders of magnitude. Although this is possible in principle (Errani et al. 2018; Genina et al. 2018), we see little justification in modelling the entire population of Milky Way satellites with a unique power law and normalization.

A clear limitation of our comparison to the results of Kaplinghat et al. (2019), especially for the population of luminous satellites, is the inability of our simulations to match the observed radial distribution of the Milky Way satellites, which is due in part to the fact that host galaxy’s baryonic disk is too small (Bose et al. 2020). To that end, comparison of the Kaplinghat et al. (2019) relation to dwarfs selected so as to match the radial distribution of the Milky Way satellites using a procedure similar to that used by Riley et al. (2019) would be more appropriate. Nevertheless, given the various selection biases and the known limitations of both the modelling techniques and the simulations we have employed here, we shall leave a more meaningful comparison of CDM+hydrodynamics simulations to the relation of Kaplinghat et al. (2019) for future work. For now, we point out that an anti-correlation of density and pericentre does exist in our simulations, reflecting ‘survivor bias’, but the slope of this relation is weak. Simulations with a more massive baryonic disk are required for a fairer comparison to the Milky Way satellites. If the power-law density-pericentre relation exists and its

slope cannot be accounted for by “survivor bias”, this may pose an interesting challenge for CDM simulations of Milky Way analogues.

5.2 What is the halo mass of Fornax?

5.2.1 Dynamical estimates

Read & Erkal (2019) fit a CORENFWTIDES model to Fornax to estimate its *pre-infall* dynamical mass, obtaining $M_{200} = 2.4^{+0.8}_{-0.5} \times 10^9 M_{\odot}$. The pre-infall values of M_{200} for our Fornax analogues lie above this estimate. However, it is challenging to dynamically estimate the halo mass out to Fornax’s virial radius ($R_{200} \sim 60 - 70$ kpc) from data near its half-light radius (~ 1 kpc) and the inferred M_{200} depends on the assumed form of the outer dark matter density profile.

Errani et al. (2018) find that cored, tidally-stripped, models for Fornax favour a higher *present-day* total mass than cuspy models (see the left panel of Fig. 9), with their cored models reaching masses up to $M_{200} = 2.5 \times 10^{10} M_{\odot}$ within their 68 per cent confidence interval, while cuspy models reach $2.5 \times 10^9 M_{\odot}$. The present-day halo masses of 4 of our Fornax analogues are consistent within 1 σ with the cuspy models of Errani et al. (2018).

5.2.2 Abundance matching

An alternative route to estimating Fornax’s pre-infall halo mass is from abundance matching. This has traditionally been done using the stellar-mass halo-mass relation ($M_* - M_{200}$), for which Fornax favours a mass $M_{200} \sim 10^{10} M_{\odot}$ (Read et al. 2017, however, see also the relation of Miller et al. 2014, who predict $M_{200} = 3.9^{+2.3}_{-1.4} \times 10^9 M_{\odot}$ for a galaxy at $z = 0.2 - 1$ with a stellar mass of Fornax, in agreement with 2 of our analogues). This value is substantially higher than the dynamical estimate of Read & Erkal 2019 (though consistent with the estimate of Errani et al. (2018) for Fornax with a large dark matter core). This tension grows worse if we account for the quenching time of Fornax ~ 2 Gyr ago, meaning this dwarf may not have formed all the stars it would have done had it remained isolated. To correct for this, Read & Erkal (2019) reformulate the halo-galaxy connection as a relation between the mean star formation rate, $\langle \text{SFR} \rangle$, and halo mass, finding an even higher $M_{200} \sim 2 \times 10^{10} M_{\odot}$.

In Read & Erkal (2019)’s analysis, the SFR is averaged over the time when the galaxy is forming stars. The inferred pre-infall M_{200} for any given galaxy is then dependent on how quenching is defined. The relation is most useful when the mean star formation rate reflects the halo mass of the galaxy (i.e. its ability to accrete and retain gas and to form stars). However, if star formation is enhanced for reasons other than halo build-up, for example, due to a passage through pericentre (Genina et al. 2018), then $\langle \text{SFR} \rangle$ could become biased if $\text{SFR}(t)$ is not truncated appropriately. The recent study of the star formation history of Fornax, using *HST* data, by Rusakov et al. (2021) supports a scenario where Fornax has had a recent (~ 5 Gyr ago) burst in star formation, which could coincide with its pericentric passage (Patel et al. 2020). In Fig. A1 of Read & Erkal (2019), it is shown that if $\text{SFR}(t)$ is truncated at around 5 Gyr ago, their $\langle \text{SFR} \rangle$ -based abundance matching method would give an M_{200} for Fornax of $\sim 7 \times 10^9 M_{\odot}$, compatible with the cuspy Fornax analogues we study here.

We also note that, by construction, the abundance matching relation of Read & Erkal (2019) does not distinguish satellites and isolated galaxies. At the stellar mass of Fornax, the relation is dominated by star-forming galaxies at $z = 0$, rather than quenched

galaxies. This is in contrast to the population of dwarfs we consider here and could explain the discrepancy between the value of the peak M_{200} inferred via abundance matching and via our hydrodynamic simulations if the halo mass of a Fornax-like isolated dwarf approximately triples between the infall time of a satellite counterpart and $z = 0$. However, we have verified that our Fornax analogues in terms of $V_{1/2}$ and M_V , which are isolated dwarfs, also have $M_{200,z=0} \lesssim 10^{10} M_{\odot}$.

Another important aspect of both the $M_* - M_{200}$ and $\langle \text{SFR} \rangle - M_{200}$ relations is the estimate of the total stellar mass (de Boer et al. 2012). Such a quantity is not measurable directly and many photometry-based efforts are susceptible to various selection and modelling biases. A lower stellar mass for Fornax ($M_* < 4.3 \times 10^7 M_{\odot}$) would also alleviate the discrepancy between the values of M_{200} predicted in our simulations and abundance-matching arguments.

Finally, it is possible that the stellar-halo mass relation in APOSTLE is not representative of the Local Group satellites. The relation is highly sensitive to the subgrid models for star formation and feedback employed in the simulations. APOSTLE uses the EAGLE-REF model (Fattahi et al. 2016b; Sawala et al. 2016), which effectively allows stars to form in lower mass haloes than the EAGLE-RECAL model (Schaye et al. 2015; Crain et al. 2015). Indeed, the latter would place a Fornax-like galaxy in a dark matter halo of $z=0$ mass $\sim 3 \times 10^{10} M_{\odot}$ (Shao et al. 2020). At such a high halo mass, the tidal stripping scenario for the reduced central density of Fornax would become far less likely (though the scatter in the relation could still permit some analogues to be identified). In this case, different subgrid models (such as those that produce feedback-induced core formation) would be required to explain the low central density in Fornax (Navarro et al. 1996a; Read & Gilmore 2005; Pontzen & Governato 2012; Benítez-Llambay et al. 2019).

5.3 How well is the pericentre of Fornax known?

The inferred pericentre depends strongly on the model of the Milky Way potential. This is evident in Fig. 1, where 7 different potentials give pericentres between ~ 25 kpc and ~ 150 kpc. These pericentres are derived from detailed models that take into account the various Milky Way components (Gaia Collaboration et al. 2018; Bajkova & Bobylev 2020). A pericentre for Fornax that is less than 50 kpc will naturally explain its low density and these pericentres are, at the moment, not ruled out. Future improvements will come from accurate mass models of the Milky Way (see Wang et al. 2020 for an extensive review), which include adiabatic contraction (Callingham et al. 2020; Cautun et al. 2020), as well as dynamical models that take into account the potentials of the Large and Small Magellanic Clouds (Patel et al. 2020) and the Milky Way halo growth (Correa et al. 2015a,b,c).

5.4 Tidal stripping in cosmological simulations

It has been recently shown by van den Bosch et al. (2018) and van den Bosch & Ogiya (2018) (see also Errani & Peñarrubia 2020) that subhaloes in N -body simulations can be subject to artificial disruption – that is, disruption due to numerical effects, rather than physical processes. This could be caused by a gravitational softening that is too large, as well as discreteness effects, resulting in a runaway instability. If our simulated subhaloes were to be tidally stripped prematurely, this could be a potential limitation to our results.

In Appendix B we show that, particularly for our Fornax analogues, we expect the change in the radius of the maximum circular velocity, R_{\max} , as a satellites orbits, to be consistent with the “tidal tracks” of Errani & Navarro (2020). We estimate that the reduction in V_{\max} could be overestimated by ~ 10 per cent. This does not change the fact that our analogues are similar to Fornax in terms of their present-day $V_{\text{circ}}(947 \text{ pc})$ (given that this quantity evolves similarly to V_{\max}). Moreover, none of our Fornax analogues lose more than ~ 90 per cent of their bound mass and they all have $> 10^5$ particles at infall. According to van den Bosch & Ogiya (2018) and Errani & Navarro (2020), enhanced tidal stripping due to numerical effects is not noticeable for subhaloes with these properties. Nevertheless, we argue that a comprehensive convergence study of the tidal disruption of haloes in a cosmological setting, with the inclusion of baryonic effects, is certainly warranted.

6 UNDERSTANDING THE LOW DARK MATTER DENSITY IN FORNAX

We now place our findings in the context of the inferred properties of the Fornax dwarf galaxy and summarise the ability of various mechanisms (or their combination) to explain these properties in Table 1.

Kinematic analyses suggest that Fornax has a low dark matter density, both in its centre and its outskirts, as compared to expectations from abundance matching in Λ CDM. One explanation for this is the formation of a dark matter core through baryonic processes. Cores can form as a consequence of dark matter ‘heating’ over time due to supernovae feedback associated with extended periods of star formation. For such a model to fit Fornax’s low density at all radii on its own, Fornax requires a dark matter core of size $\sim 1 \text{ kpc}$ and density $\sim 5 \times 10^7 M_{\odot} \text{ kpc}^{-3}$. In this scenario, Fornax inhabits a halo with a high pre-infall mass, of order $M_{200,\text{dyn}} \sim 1 - 2 \times 10^{10} M_{\odot}$, consistent with the value inferred from abundance matching $M_{200, \langle \text{SFR} \rangle}$ (see Section 5.2 and Read & Erkal 2019).

Alternatively, Fornax could inhabit a cuspy dark matter halo, with its low density owing entirely to tides. This can occur if Fornax is on a low pericentre orbit around the Milky Way, or if it experienced tidal interactions with other galaxies prior to infall. This scenario requires Fornax’s pre-infall $M_{200,\text{dyn}}$ to be significantly lower than that inferred from abundance matching with star formation rate. Abundance matching can return a pre-infall $M_{200, \langle \text{SFR} \rangle}$ that is biased high if Fornax’s stellar mass is overestimated, if its SFR was boosted due to its interaction with the Milky Way, or if the abundance matching relations we have used in this paper are not appropriate for satellites like Fornax (see Section 5.2). We note that the analysis of HST data by Rusakov et al. (2021) suggests an SFR boost in Fornax 5 Gyr ago, which may coincide with its orbital pericentre (see the right panel of Fig. 2). Cuspy profiles are still at $> 2\sigma$ tension with the kinematics of Fornax below $R_{1/2}$ (see Fig. 8), however. A core in these regions, created through dark matter heating by supernovae feedback, for example, would provide a better agreement with the data.

We note that the analysis of Genina et al. (2020) has shown that the deviations from a $\rho \propto r^{-1}$ cusp of the inferred density profile of Fornax from Read et al. (2019), who used a broken-power-law dark matter density model, is at present consistent with the bias expected in spherical Jeans analysis when modelling an elliptical galaxy (with a Fornax-like on-the-sky ellipticity $e = 0.3$) inside a cuspy CDM halo that is viewed along its minor or intermediate

axis. As demonstrated in Fig. 9, all of our Fornax analogues are consistent with the axisymmetric Jeans analysis of Hayashi et al. (2020) within the 95 per cent confidence levels. Analysis using larger spectroscopic samples will clarify whether ellipticity could be the culprit for Fornax’s inferred density profile shape.

In the end, Fornax’s low density may owe to some combination of all of the above effects. To determine whether tides have played a role, we can hunt for Fornax’s stream of unbound stars. While signs of tidal stripping in Fornax have not yet been detected (Walker et al. 2006; Wang et al. 2019b), we showed in this work that the tidal tails, if present, are expected to be seen over an area of $\sim 100 \text{ deg}^2$ with a surface brightness of $\sim 35 - 36 \text{ mag arcsec}^{-2}$. Such tidal tails should be detectable in future surveys, if tidal effects are responsible – wholly or in part – for lowering the dark matter density in Fornax.

Finally, a dark matter core in Fornax has been previously invoked as a solution to the globular cluster survivability problem (Goerdt et al. 2006; Cole et al. 2012). In a cuspy halo, the globular clusters are expected to rapidly sink to the centre of the dwarf, while in a halo with a core the globular clusters would stall at approximately the core radius (Cole et al. 2012). The survival of globular clusters in Fornax at the present day is thus suggestive of a core in this galaxy. Note, however, that such timing arguments cannot conclusively rule out a cusp (Cole et al. 2012; Meadows et al. 2020; Shao et al. 2020). In the context of our work here, if tides are important for Fornax after all, we can actually re-ignite the original solution to the ‘timing problem’ for Fornax’s globular clusters whereby their infall is delayed purely by tidal effects (Oh et al. 2000).

7 SUMMARY AND CONCLUSIONS

Fornax is one of the largest and brightest dwarf satellites of the Milky Way, making it a prime target for spectroscopic and photometric studies that over the years have provided an abundance of data. In particular, measurements of the motions of individual stars in Fornax have been used to place constraints on its underlying gravitational potential. For example, Read et al. (2019) have found that Fornax must have a low inner dark matter density, which could be a signature of a dark matter ‘core’ in its central regions.

In this work, we have tested an alternative scenario in which the low inferred density in Fornax is due to tidal effects. This was disfavoured by Read et al. (2019), who argued that the proper motions, star formation history and inferred pre-infall halo mass of Fornax are inconsistent with this interpretation. We tested this on a large sample of dwarf galaxies selected from the APOSTLE suite of cosmological N -body hydrodynamic simulations in Local Group-like environments. We find the following:

- We confirm that the star formation history of Fornax is consistent with that of a dwarf galaxy that is a satellite of the Milky Way in our simulations (see right panel of Fig. 2).
- Close matches to Fornax in *both* visible magnitude, M_V , and circular velocity at the half-light radius, $V_{\text{circ}}(947 \text{ pc})$, are quite rare in our simulations (see left panel of Fig. 2); however we find 9 Fornax analogues (2 of which are particularly close matches). These analogues also have inferred orbital apo- and pericentres compatible with Fornax data (Gaia Collaboration et al. 2018; Fritz et al. 2018; Li et al. 2021).
- By examining mass loss from dwarf galaxies with orbital properties consistent with those measured for Fornax, we show that,

Table 1. The effectiveness of various physical mechanisms, within the CDM framework, in explaining the properties of the Fornax dwarf spheroidal, including dynamical properties inferred by [Read et al. \(2019\)](#) and [Read & Erkal \(2019\)](#), and globular cluster (GC) survival. For each scenario we also include the prospect for detecting tidal tails.

Reason for low density	$\rho (< R_{1/2})$	Density profile shape	SFR enhanced?	$M_{200,\text{dyn}} = M_{200,(\text{SFR})}$	Globular cluster survival	Tidal tails?
DM heating alone	Yes	Core / Shallow cusp	No	Yes (for \sim kpc cores)	Yes	No
Strong Tides alone	Yes	Cuspy, disfavoured at $\geq 2\sigma$	Maybe	(SFR boost required)	Yes	Yes
DM heating + Strong Tides	Yes	Core / Shallow cusp	Maybe	(SFR boost required)	Yes	Yes
DM heating + Strong Tides + SFR boost	Yes	Core / Shallow cusp	Yes	Yes	Yes	Yes

even at large present-day pericentres, dwarf satellites can suffer significant mass loss. We find that, for galaxies on Fornax-like orbits (independently of mass), 26 per cent lose more than 50 per cent of their mass within 1 kpc (see Fig. 3).

- We explore the relevance of the star formation history to the degree to which a dwarf has experienced tidal effects. We show that in many cases the quenching time is directly related to the infall time; however, there exists a population of galaxies with similar stellar mass to Fornax, or larger, that are quenched long after infall. This is because they are able to preserve their gas supply after infall and, in extreme cases, even after multiple orbital pericentres (see the left panel of Fig. 4).

- We find that in ~ 37 per cent of simulated dwarf satellites with orbits similar to Fornax, mass loss begins more than 2 Gyr prior to infall. As such, the infall time is not always a reliable estimate of the time at which the dwarf had its maximum mass (see right panel of Fig. 4). By examining individual Fornax analogues, we found that, in some cases, dwarfs can lose mass prior to infall due to interactions with more massive dwarf galaxies, perhaps due to infall as part of a group or a fly-by. Two consecutive fly-bys are responsible for the tidal stripping of one of our best Fornax analogues (the ‘star’ Fornax on the left side of Fig. 5).

- We emphasize that if cores do not form through baryonic feedback in CDM, the low density in Fornax must be due to tidal effects. Although one of our Fornax analogues is a weakly stripped low-mass halo (‘thick diamond’ analogue), its density profile is discrepant at 3σ from the density profile inferred for Fornax by [Read et al. \(2019\)](#) and, unlike Fornax, this galaxy retains ~ 25 per cent of its all-time maximum gas content at $z = 0$ ([Spekkens et al. 2014](#)). If Fornax was stripped to a similar extent as our best analogue, its tidal tails should be visible with a surface brightness limit of $\sim 35 - 36$ mag arcsec² and a survey area of ≥ 100 deg² (see Fig. 6), which has not been presently achieved with surveys like DES ([Wang et al. 2019b](#)). We also show that the proper motions and line-of-sight velocities of the stars in the tidal tails peak at the same values as the bound stars (see Fig. 7). Similarly to Fornax, our best analogue also exhibits a metallicity gradient ([Kirby et al. 2010](#)), leading to the tidal tails which are

typically more metal-poor than Milky Way halo stars. These properties could aid the detection of the tidal tails of Fornax in the future.

- By comparing the density profiles of our Fornax analogues to that derived for Fornax by [Read et al. \(2019\)](#), we show that a NFW profile shape is consistent with Fornax within 3σ in the radial range 0.1 - 2 kpc, while Einasto profiles, with shallower inner cusps, are consistent within $2-3\sigma$ levels. A much better fit to the data is obtained for a stripped dwarf with a rather shallow cusp or core that could have been created by dark matter heating (see Fig. 8). Our Fornax analogues all have higher values of ρ_{150} than inferred by [Read et al. \(2019\)](#), with only two dwarfs consistent with Fornax within 2σ and 5 consistent within 3σ . We note, however, that all of the analogues have values of ρ_{150} consistent with the result for Fornax from [Hayashi et al. \(2020\)](#) within 2σ .

- We apply the analysis of [Read et al. \(2019\)](#), based on the inner densities and pre-infall halo masses of dwarfs, to our Fornax analogues. We show that a number of dwarfs with similar V_{circ} (947 pc) and M_V to Fornax, and pericentres between 20 and 120 kpc, have central densities comparable to that of Fornax (see Fig. 9). It is clear that there exist dwarf satellites in our simulations, with orbits similar to Fornax, that have been tidally stripped more extensively than their pericentres would suggest. We note, however, that a small (< 50 kpc) pericentre for Fornax is not ruled out at present.

- Our simulation results are at odds with the inference by [Read & Erkal \(2019\)](#) of the pre-infall halo mass of Fornax. The simulations imply that a galaxy with the present-day properties of Fornax should have a pre-infall halo mass of $(4-9) \times 10^9 M_{\odot}$, while [Read & Erkal \(2019\)](#) infer $2 \times 10^{10} M_{\odot}$. One possible explanation for this is that Fornax’s star formation was enhanced on infall to the Milky Way. This would raise its $\langle \text{SFR} \rangle$, leading [Read & Erkal \(2019\)](#) to overestimate Fornax’s pre-infall mass. Alternatively, it may be that APOSTLE provides an inadequate representation of the stellar-to-halo or the $\langle \text{SFR} \rangle$ -to-halo mass relation on Fornax scales.

- We show that the central densities and pericentric distances of satellite dwarfs in our simulations are, at present, compatible with

the anti-correlation between these properties in Milky Way satellites highlighted by [Kaplinghat et al. \(2019\)](#). The anti-correlation in our simulations exists due to the “survivor bias”, but is relatively weak. The slope of the anti-correlation must be confirmed using Milky Way simulations with a more massive baryonic disk. At present, the limitations of our simulations as well as selection biases and modelling techniques involved in computing the relevant properties for the Milky Way satellites make a direct comparison with [Kaplinghat et al. \(2019\)](#) non-trivial and we shall therefore leave this for future work.

In conclusion, we have shown in this work that tides can play an important role in the evolutionary history of Milky Way satellite galaxies, even if that may not be obvious from their present-day orbital pericentres. We have focused on the Fornax dwarf galaxy and have explicitly shown that in CDM simulations in which cores do not form by baryonic processes, the low dark matter density in Fornax can only be explained by Galactic tides. As such, a failure to detect stellar streams associated with Fornax could rule out such models. With regards to the density profile itself, our analysis suggests that the most stringent test of the cusp vs. core dichotomy will come from an accurate inference of the dark matter density profile on ~ 100 pc scales. At present, a low-density NFW profile in Fornax cannot be ruled out, although the data do seem to favour a shallow cusp or core. More precise determinations of the dark matter distribution of Fornax may become possible with more radial velocities in the inner 100-200 pc, long-baseline proper motion measurements for individual stars with *Gaia* and *HST* ([Massari et al. 2018](#); [Strigari et al. 2018b](#)), accounting for asymmetry ([Hayashi et al. 2020](#)) and rotation ([Zhu et al. 2016b](#)), and consideration of independent constraints from its multiple stellar populations ([Walker & Peñarrubia 2011](#)).

ACKNOWLEDGEMENTS

We thank an anonymous referee for a detailed reading of our paper and for several suggestions that helped us improve it. AG and JR would like to thank the organizers of the “5th Gaia Challenge” workshop, where this work originated. This work was supported by the Science and Technology Facilities Council (STFC) consolidated grant ST/T000244/1. AG acknowledges an STFC studentship grant ST/N50404X/1 and the Ogden Scholarship Fund. AF acknowledges support by the STFC [grant number ST/P000541/1] and the Leverhulme Trust. CSF acknowledges support by the European Research Council (ERC) through Advanced Investigator grant DMIDAS (GA 786910). This work used the DiRAC Data Centric system at Durham University, operated by the Institute for Computational Cosmology on behalf of the STFC DiRAC HPC Facility (www.dirac.ac.uk). This equipment was funded by BIS National E-infrastructure capital grant ST/K00042X/1, STFC capital grant ST/H008519/1, and STFC DiRAC Operations grant ST/K003267/1 and Durham University. DiRAC is part of the National E-Infrastructure. This work has benefited from the use of NUMPY, SCIPY and MATPLOTLIB.

DATA AVAILABILITY

The data analysed in this article can be made available upon reasonable request to the corresponding author.

REFERENCES

- Adams J. J., et al., 2014, *ApJ*, **789**, 63
- Agnello A., Evans N. W., 2012, *ApJ*, **754**, L39
- Amorisco N. C., Evans N. W., 2012, *MNRAS*, **419**, 184
- Amorisco N. C., Agnello A., Evans N. W., 2013, *MNRAS*, **429**, L89
- Amorisco N. C., Zavala J., de Boer T. J. L., 2014, *ApJ*, **782**, L39
- Bajkova A. T., Bobylev V. V., 2020, arXiv e-prints, p. [arXiv:2007.02350](https://arxiv.org/abs/2007.02350)
- Bate N. F., McMonigal B., Lewis G. F., Irwin M. J., Gonzalez-Solares E., Shanks T., Metcalfe N., 2015, *MNRAS*, **453**, 690
- Battaglia G., et al., 2006, *A&A*, **459**, 423
- Battaglia G., Helmi A., Tolstoy E., Irwin M., Hill V., Jablonka P., 2008, *ApJ*, **681**, L13
- Battaglia G., Sollima A., Nipoti C., 2015, *MNRAS*, **454**, 2401
- Benítez-Llambay A., Frenk C. S., Ludlow A. D., Navarro J. F., 2019, *MNRAS*, **488**, 2387
- Binney J., Tremaine S., 1987, Galactic dynamics. Princeton University Press
- Boldrini P., Mohayaee R., Silk J., 2019, *MNRAS*, **485**, 2546
- Borukhovetskaya A., Errani R., Navarro J. F., Fattahi A., Santos-Santos I., 2021, arXiv e-prints, p. [arXiv:2104.00011](https://arxiv.org/abs/2104.00011)
- Bose S., et al., 2019, *MNRAS*, **486**, 4790
- Bose S., Deason A. J., Belokurov V., Frenk C. S., 2020, *MNRAS*, **495**, 743
- Bovy J., 2015, *ApJS*, **216**, 29
- Bruzual G., Charlot S., 2003, *MNRAS*, **344**, 1000
- Bullock J. S., Boylan-Kolchin M., 2017, *ARA&A*, **55**, 343
- Callingham T. M., Cautun M., Deason A. J., Frenk C. S., Grand R. J. J., Marinacci F., Pakmor R., 2020, *MNRAS*, **495**, 12
- Campbell D. J. R., et al., 2017, *MNRAS*, **469**, 2335
- Cautun M., et al., 2020, *MNRAS*, **494**, 4291
- Cole D. R., Dehnen W., Read J. I., Wilkinson M. I., 2012, *MNRAS*, **426**, 601
- Coleman M. G., Da Costa G. S., 2005, *Publ. Astron. Soc. Australia*, **22**, 162
- Coleman M., Da Costa G. S., Bland-Hawthorn J., Martínez-Delgado D., Freeman K. C., Malin D., 2004, *AJ*, **127**, 832
- Coleman M. G., Da Costa G. S., Bland-Hawthorn J., Freeman K. C., 2005, *AJ*, **129**, 1443
- Correa C. A., 2020, arXiv e-prints, p. [arXiv:2007.02958](https://arxiv.org/abs/2007.02958)
- Correa C. A., Wyithe J. S. B., Schaye J., Duffy A. R., 2015a, *MNRAS*, **450**, 1514
- Correa C. A., Wyithe J. S. B., Schaye J., Duffy A. R., 2015b, *MNRAS*, **450**, 1521
- Correa C. A., Wyithe J. S. B., Schaye J., Duffy A. R., 2015c, *MNRAS*, **452**, 1217
- Crain R. A., et al., 2015, *MNRAS*, **450**, 1937
- D’Onghia E., Springel V., Hernquist L., Keres D., 2010, *ApJ*, **709**, 1138
- Davis M., Efstathiou G., Frenk C. S., White S. D. M., 1985, *ApJ*, **292**, 371
- Del Popolo A., Le Delliou M., 2017, *Galaxies*, **5**, 17
- Di Cintio A., Knebe A., Libeskind N. I., Brook C., Yepes G., Gottlöber S., Hoffman Y., 2013, *MNRAS*, **431**, 1220
- Digby R., et al., 2019, *MNRAS*, **485**, 5423
- Dutton A. A., Macciò A. V., 2014, *MNRAS*, **441**, 3359
- Dutton A. A., Macciò A. V., Buck T., Dixon K. L., Blank M., Obreja A., 2019, *MNRAS*, **486**, 655
- Elbert O. D., Bullock J. S., Garrison-Kimmel S., Rocha M., Oñorbe J., Peter A. H. G., 2015, *MNRAS*, **453**, 29
- Errani R., Navarro J. F., 2020, arXiv e-prints, p. [arXiv:2011.07077](https://arxiv.org/abs/2011.07077)
- Errani R., Peñarrubia J., 2020, *MNRAS*, **491**, 4591
- Errani R., Peñarrubia J., Walker M. G., 2018, *MNRAS*, **481**, 5073
- Fattahi A., Navarro J. F., Sawala T., Frenk C. S., Sales L. V., Oman K., Schaller M., Wang J., 2016a, arXiv e-prints, p. [arXiv:1607.06479](https://arxiv.org/abs/1607.06479)
- Fattahi A., et al., 2016b, *MNRAS*, **457**, 844
- Fattahi A., Navarro J. F., Frenk C. S., Oman K. A., Sawala T., Schaller M., 2018, *MNRAS*, **476**, 3816
- Fillingham S. P., et al., 2019, arXiv e-prints, p. [arXiv:1906.04180](https://arxiv.org/abs/1906.04180)
- Fitts A., et al., 2017, *MNRAS*, **471**, 3547
- Flores R. A., Primack J. R., 1994, *ApJ*, **427**, L1
- Fritz T. K., Battaglia G., Pawłowski M. S., Kallivayalil N., van der Marel R., Sohn S. T., Brook C., Besla G., 2018, *A&A*, **619**, A103

- Gaia Collaboration et al., 2018, *A&A*, **616**, A12
- Gaia Collaboration Brown A. G. A., Vallenari A., Prusti T., de Bruijne J. H. J., Babusiaux C., Biermann M., 2020, arXiv e-prints, p. [arXiv:2012.01533](https://arxiv.org/abs/2012.01533)
- Genina A., et al., 2018, *MNRAS*, **474**, 1398
- Genina A., Frenk C. S., Benítez-Llambay A. r., Cole S., Navarro J. F., Oman K. A., Fattahi A., 2019, *MNRAS*, **488**, 2312
- Genina A., et al., 2020, *MNRAS*, **498**, 144
- Goerdt T., Moore B., Read J. I., Stadel J., Zemp M., 2006, *MNRAS*, **368**, 1073
- Governato F., et al., 2012, *MNRAS*, **422**, 1231
- Grand R. J. J., et al., 2017, *MNRAS*, **467**, 179
- Green S. B., van den Bosch F. C., 2019, *MNRAS*, **490**, 2091
- Han J., Cole S., Frenk C. S., Benitez-Llambay A., Helly J., 2018, *MNRAS*, **474**, 604
- Hayashi K., Chiba M., Ishiyama T., 2020, arXiv e-prints, p. [arXiv:2007.13780](https://arxiv.org/abs/2007.13780)
- Hirtenstein J., et al., 2019, *ApJ*, **880**, 54
- Hopkins P. F., 2013, *MNRAS*, **428**, 2840
- Hui L., Ostriker J. P., Tremaine S., Witten E., 2017, *Phys. Rev. D*, **95**, 043541
- Irrgang A., Wilcox B., Tucker E., Schiefelbein L., 2012, *A&A*, **549**, A137
- Jardel J. R., Gebhardt K., 2012, *ApJ*, **746**, 89
- Kaplinghat M., Valli M., Yu H.-B., 2019, *MNRAS*, **490**, 231
- Kauffmann G., 2014, *MNRAS*, **441**, 2717
- Kelly A. J., Jenkins A., Deason A., Fattahi A., Grand R. J. J., Pakmor R., Springel V., Frenk C. S., 2021a, arXiv e-prints, p. [arXiv:2106.08618](https://arxiv.org/abs/2106.08618)
- Kelly A. J., Jenkins A., Frenk C. S., 2021b, *MNRAS*, **502**, 2934
- Kirby E. N., Lanfranchi G. A., Simon J. D., Cohen J. G., Guhathakurta P., 2010, *ApJ*, **727**, 78
- Kirby E. N., Boylan-Kolchin M., Cohen J. G., Geha M., Bullock J. S., Kaplinghat M., 2013a, *ApJ*, **770**, 16
- Kirby E. N., Cohen J. G., Guhathakurta P., Cheng L., Bullock J. S., Gallazzi A., 2013b, *ApJ*, **779**, 102
- Kirby E. N., Cohen J. G., Simon J. D., Guhathakurta P., Thygesen A. O., Duggan G. E., 2017, *ApJ*, **838**, 83
- Komatsu E., et al., 2011, *ApJS*, **192**, 18
- Kuzio de Naray R., McGaugh S. S., de Blok W. J. G., Bosma A., 2006, *ApJS*, **165**, 461
- Lancaster L., Giovanetti C., Mocz P., Kahn Y., Lisanti M., Spergel D. N., 2020, *J. Cosmology Astropart. Phys.*, **2020**, 001
- Leaman R., et al., 2012, *ApJ*, **750**, 33
- Lemasle B., et al., 2014, *A&A*, **572**, A88
- Letarte B., et al., 2010, *A&A*, **523**, A17
- Leung G. Y. C., Leaman R., van de Ven G., Battaglia G., 2020, *MNRAS*, **493**, 320
- Li H., Hammer F., Babusiaux C., Pawlowski M. S., Yang Y., Arenou F., Du C., Wang J., 2021, arXiv e-prints, p. [arXiv:2104.03974](https://arxiv.org/abs/2104.03974)
- Licquia T. C., Newman J. A., 2015, *ApJ*, **806**, 96
- Lokas E. L., 2002, *MNRAS*, **333**, 697
- Lokas E. L., Kazantzidis S., Majewski S. R., Law D. R., Mayer L., Frinchaboy P. M., 2010, *ApJ*, **725**, 1516
- Ludlow A. D., Schaye J., Bower R., 2019, *MNRAS*, **488**, 3663
- Lux H., Read J. I., Lake G., 2010, *MNRAS*, **406**, 2312
- Mashchenko S., Wadsley J., Couchman H. M. P., 2008, *Science*, **319**, 174
- Massari D., Breddels M. A., Helmi A., Posti L., Brown A. G. A., Tolstoy E., 2018, *Nature Astronomy*, **2**, 156
- McConnachie A. W., 2012, *AJ*, **144**, 4
- McMillan P. J., 2016, *MNRAS*, **465**, 76
- Meadows N., Navarro J. F., Santos-Santos I., Benítez-Llambay A., Frenk C., 2020, *MNRAS*, **491**, 3336
- Miller M. J., Bregman J. N., 2015, *ApJ*, **800**, 14
- Miller S. H., Ellis R. S., Newman A. B., Benson A., 2014, *ApJ*, **782**, 115
- Mo H., van den Bosch F. C., White S., 2010, *Galaxy Formation and Evolution*. Cambridge University Press
- Moore B., 1994, *Nature*, **370**, 629
- Navarro J. F., Eke V. R., Frenk C. S., 1996a, *MNRAS*, **283**, L72
- Navarro J. F., Frenk C. S., White S. D. M., 1996b, *ApJ*, **462**, 563
- Navarro J. F., Frenk C. S., White S. D. M., 1997, *ApJ*, **490**, 493
- Navarro J. F., et al., 2010, *MNRAS*, **402**, 21
- Neto A. F., et al., 2007, *MNRAS*, **381**, 1450
- Newville M., Stensitzki T., Allen D. B., Rawlik M., Ingargiola A., Nelson A., 2016, *Lmfit: Non-Linear Least-Square Minimization and Curve-Fitting for Python* (ascl:1606.014)
- Oñorbe J., Boylan-Kolchin M., Bullock J. S., Hopkins P. F., Kereš D., Faucher-Giguère C.-A., Quataert E., Murray N., 2015, *MNRAS*, **454**, 2092
- Oh K. S., Lin D. N. C., Richer H. B., 2000, *ApJ*, **531**, 727
- Oh S.-H., de Blok W. J. G., Walter F., Brinks E., Kennicutt Robert C. J., 2008, *AJ*, **136**, 2761
- Oh S.-H., et al., 2015, *AJ*, **149**, 180
- Orkney M. D. A., Read J. I., Petts J. A., Gieles M., 2019, *MNRAS*, **488**, 2977
- Pascale R., Posti L., Nipoti C., Binney J., 2018, *MNRAS*, **480**, 927
- Patel E., et al., 2020, *ApJ*, **893**, 121
- Peñarrubia J., Navarro J. F., McConnachie A. W., Martin N. F., 2009, *ApJ*, **698**, 222
- Peñarrubia J., Benson A. J., Walker M. G., Gilmore G., McConnachie A. W., Mayer L., 2010, *MNRAS*, **406**, 1290
- Percival W. J., et al., 2001, *MNRAS*, **327**, 1297
- Pontzen A., Governato F., 2012, *MNRAS*, **421**, 3464
- Pouliasis E., Di Matteo P., Haywood M., 2017, *A&A*, **598**, A66
- Power C., Navarro J. F., Jenkins A., Frenk C. S., White S. D. M., Springel V., Stadel J., Quinn T., 2003, *MNRAS*, **338**, 14
- Read J. I., Erkal D., 2019, *MNRAS*, **487**, 5799
- Read J. I., Gilmore G., 2005, *MNRAS*, **356**, 107
- Read J. I., Steger P., 2017, *MNRAS*, **471**, 4541
- Read J. I., Wilkinson M. I., Evans N. W., Gilmore G., Kleyna J. T., 2006, *MNRAS*, **367**, 387
- Read J. I., Agertz O., Collins M. L. M., 2016, *MNRAS*, **459**, 2573
- Read J. I., Iorio G., Agertz O., Fraternali F., 2017, *MNRAS*, **467**, 2019
- Read J. I., Walker M. G., Steger P., 2018, *MNRAS*, **481**, 860
- Read J. I., Walker M. G., Steger P., 2019, *MNRAS*, **484**, 1401
- Retana-Montenegro E., van Hese E., Gentile G., Baes M., Frutos-Alfaro F., 2012, *A&A*, **540**, A70
- Richardson T., Fairbairn M., 2013, arXiv e-prints, p. [arXiv:1305.0670](https://arxiv.org/abs/1305.0670)
- Richings J., et al., 2020, *MNRAS*, **492**, 5780
- Riley A. H., et al., 2019, *MNRAS*, **486**, 2679
- Robin A. C., Reylé C., Derrière S., Picaud S., 2003, *A&A*, **409**, 523
- Robin A. C., Marshall D. J., Schultheis M., Reylé C., 2012, *A&A*, **538**, A106
- Rocha M., Peter A. H. G., Bullock J., 2012, *MNRAS*, **425**, 231
- Rusakov V., Monelli M., Gallart C., Fritz T. K., Ruiz-Lara T., Bernard E. J., Cassisi S., 2021, *MNRAS*, **502**, 642
- Sanders J. L., Evans N. W., 2020, *MNRAS*,
- Sanders J. L., Evans N. W., Dehnen W., 2018, *MNRAS*, **478**, 3879
- Santos-Santos I. M. E., Fattahi A., Sales L. V., Navarro J. F., 2021, *MNRAS*, **504**, 4551
- Savitzky A., Golay M. J. E., 1964, *Analytical Chemistry*, **36**, 1627
- Sawala T., et al., 2016, *MNRAS*, **457**, 1931
- Sawala T., Pihajoki P., Johansson P. H., Frenk C. S., Navarro J. F., Oman K. A., White S. D. M., 2017, *MNRAS*, **467**, 4383
- Schaye J., et al., 2015, *MNRAS*, **446**, 521
- Shao S., Cautun M., Frenk C. S., Reina-Campos M., Deason A. J., Crain R. A., Kruijssen J. M. D., Pfeffer J., 2020, arXiv e-prints, p. [arXiv:2012.08058](https://arxiv.org/abs/2012.08058)
- Sparre M., Hayward C. C., Feldmann R., Faucher-Giguère C.-A., Muratov A. L., Kereš D., Hopkins P. F., 2017, *MNRAS*, **466**, 88
- Spekkens K., Urbancic N., Mason B. S., Willman B., Aguirre J. E., 2014, *ApJ*, **795**, L5
- Spergel D. N., Steinhardt P. J., 2000, *Physical Review Letters*, **84**, 3760
- Springel V., 2005, *MNRAS*, **364**, 1105
- Springel V., et al., 2005, *Nature*, **435**, 629
- Springel V., et al., 2008, *MNRAS*, **391**, 1685
- Starkenburger E., et al., 2010, *A&A*, **513**, A34
- Strigari L. E., Bullock J. S., Kaplinghat M., Kravtsov A. V., Gnedin O. Y., Abazajian K., Klypin A. A., 2006, *ApJ*, **652**, 306
- Strigari L. E., Frenk C. S., White S. D. M., 2018a, *ApJ*, **860**, 56

- Strigari L. E., Frenk C. S., White S. D. M., 2018b, *ApJ*, **860**, 56
 Tegmark M., et al., 2004, *Phys. Rev. D*, **69**, 103501
 Teyssier R., Pontzen A., Dubois Y., Read J. I., 2013, *MNRAS*, **429**, 3068
 Tollet E., et al., 2016, *MNRAS*, **456**, 3542
 Vasiliev E., Belokurov V., 2020, *MNRAS*, **497**, 4162
 Walker M. G., Peñarrubia J., 2011, *ApJ*, **742**, 20
 Walker M. G., Mateo M., Olszewski E. W., Bernstein R., Wang X., Woodroffe M., 2006, *AJ*, **131**, 2114
 Walker M. G., Mateo M., Olszewski E. W., 2008, *ApJ*, **688**, L75
 Walker M. G., Mateo M., Olszewski E. W., 2009, *AJ*, **137**, 3100
 Wang M.-Y., Strigari L. E., Lovell M. R., Frenk C. S., Zentner A. R., 2016, *MNRAS*, **457**, 4248
 Wang M. Y., et al., 2017, *MNRAS*, **468**, 4887
 Wang J., Bose S., Frenk C. S., Gao L., Jenkins A., Springel V., White S. D. M., 2019a, arXiv e-prints, p. arXiv:1911.09720
 Wang M. Y., et al., 2019b, *ApJ*, **881**, 118
 Wang W., Han J., Cautun M., Li Z., Ishigaki M. N., 2020, *Science China Physics, Mechanics, and Astronomy*, **63**, 109801
 Weinberg D. H., Bullock J. S., Governato F., Kuzio de Naray R., Peter A. H. G., 2015, *Proceedings of the National Academy of Science*, **112**, 12249
 Weisz D. R., Dolphin A. E., Skillman E. D., Holtzman J., Gilbert K. M., Dalcanton J. J., Williams B. F., 2014, *ApJ*, **789**, 147
 Wolf J., Martinez G. D., Bullock J. S., Kaplinghat M., Geha M., Muñoz R. R., Simon J. D., Avedo F. F., 2010, *MNRAS*, **406**, 1220
 Zhu Q., Marinacci F., Maji M., Li Y., Springel V., Hernquist L., 2016a, *MNRAS*, **458**, 1559
 Zhu L., van de Ven G., Watkins L. L., Posti L., 2016b, *MNRAS*, **463**, 1117
 de Blok W. J. G., 2010, *Advances in Astronomy*, **2010**, 789293
 de Boer T. J. L., et al., 2012, *A&A*, **544**, A73
 del Pino A., Aparicio A., Hidalgo S. L., 2015, *MNRAS*, **454**, 3996
 van den Bosch F. C., Ogiya G., 2018, *MNRAS*, **475**, 4066
 van den Bosch F. C., Ogiya G., Hahn O., Burkert A., 2018, *MNRAS*, **474**, 3043

APPENDIX A: SPHERICAL APPROXIMATION TO THE POTENTIAL

In this Appendix we show that the spherical approximation to the gravitational potential of APOSTLE haloes is a valid one. From our sample of satellite galaxies, we select those which have already reached their first pericentre. For this sample, we interpolate the orbits using a cubic spline. For the dwarfs which have most recently passed through an apocentre we compare the apocentric distance derived using Equation 2 ($r_{\text{apo},\text{sph}}$) with the value obtained using cubic interpolation (r_{apo}). For those that have most recently passed through a pericentre, we compare the pericentre values. The comparison is shown in Fig. A1, where it is clear that the pericentres (black) and apocentres (blue), derived using the spherical approximation of the potential, follow a one-to-one relation (red dashed line) with the ‘true’ values. There are some noticeable outliers, which correspond to recent galaxy interactions, however, these do not affect the conclusions of this work. Fig. A1 suggests that the values of the peri and apo-centres derived using the spherical approximation are a good reflection of the true values for these dwarfs.

APPENDIX B: THE ‘TIDAL TRACKS’ OF COSMOLOGICAL SUBHALOES

In this Appendix we briefly consider how our results could be affected by numerical artefacts. In particular, we wish to know if subhaloes in our simulations are stripped too fast, compared to the predictions of higher-resolution idealized models in the works of

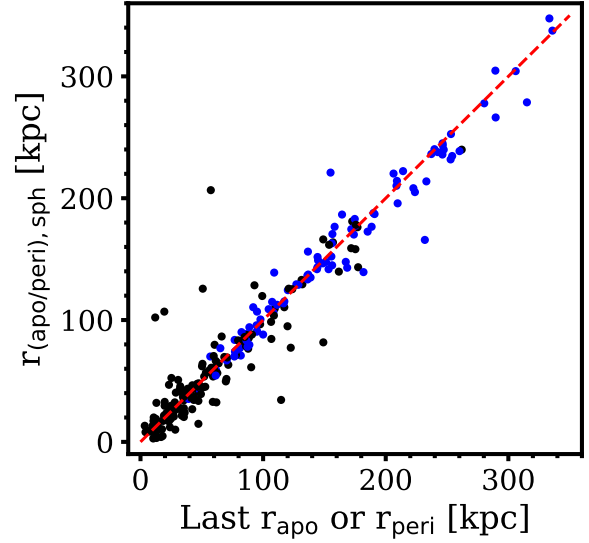


Figure A1. The apo- and peri-centres derived for satellite dwarfs in our sample using a spherical potential approximation, as a function of the corresponding last apo- or peri-centre (computed using cubic-spline orbit interpolation). The dwarfs which recently passed through their apocentre are shown in blue and those that have recently passed through their pericentre are shown in black. The red dashed line is the one-to-one relation. Only the satellites which have passed through their first pericentre are included.

Peñarrubia et al. (2010); van den Bosch & Ogiya (2018); Green & van den Bosch (2019); Errani & Navarro (2020). We note, however, that it is not clear that the results in those papers should directly translate to cosmological hydrodynamics simulations.

Motivated by the analysis of Green & van den Bosch (2019), on the left panel of Fig. B1, we show the fractional change in the maximum circular velocity, $V_{\text{max}}/V_{\text{max},0}$, and the radius of the maximum circular velocity, $R_{\text{max}}/R_{\text{max},0}$, compared to the predictions of Errani & Navarro (2020) for a given fraction of mass lost within R_{max} , $M_{\text{max}}/M_{\text{max},0}$. The reference values are set at the time of maximum M_{max} . Since the V_{max} and R_{max} evolution can be noisy in simulations due to merger and accretion history, interactions with the host galaxy and the particulars of the subhalo finders, we smooth the V_{max} and R_{max} histories of the dwarfs with a 1^{st} order Savitzky-Golay filter over 5 snapshots (Savitzky & Golay 1964). The reaction of the circular velocity profile to tidal mass loss in our simulated haloes is generally consistent with the predictions of Errani & Navarro (2020), although the scatter is visibly large and concentration-dependent. Our Fornax analogues, however, clearly deviate from the tracks and from the full sample. Some of this may be due to higher concentration of some of these dwarfs. Additionally, it is clear from the left panel of Fig. 2 that our analogues correspond to a biased selection in V_{max} for a given stellar mass. Nevertheless, considering that the bias in V_{max} is no more than 20 per cent, our Fornax analogues are still consistent with the value of V_{circ} (947 pc) of Fornax (assuming that this changes similarly to V_{max}).

It should be noted that the above is only a conservative estimate of the effects of artificial disruption on our simulated Fornax analogues. An interesting feature of Fig. B1 is that the reduction in R_{max} and V_{max} is clearly dependent on halo concentration, c_{200} (identified by the colour of the symbols in Fig. B1). This is consistent with the results of Green & van den Bosch (2019). Moreover, Errani & Navarro (2020) point out that the behaviour of the ‘tidal track’ is orbit-dependent, so we do expect some scatter about their

median relation. We also note that our Fornax analogues satisfy the force softening and number of particles criteria of [van den Bosch & Ogiya \(2018\)](#), which these authors suggest leads to an evolution of bound mass accurate to 0.1 dex. Furthermore, it has been shown that tidal tracks of aspherical haloes deviate from the spherical cases explored in [van den Bosch & Ogiya 2018](#) and [Errani & Navarro 2020](#) ([Sanders et al. 2018](#)).

This paper has been typeset from a $\text{\TeX}/\text{\LaTeX}$ file prepared by the author.

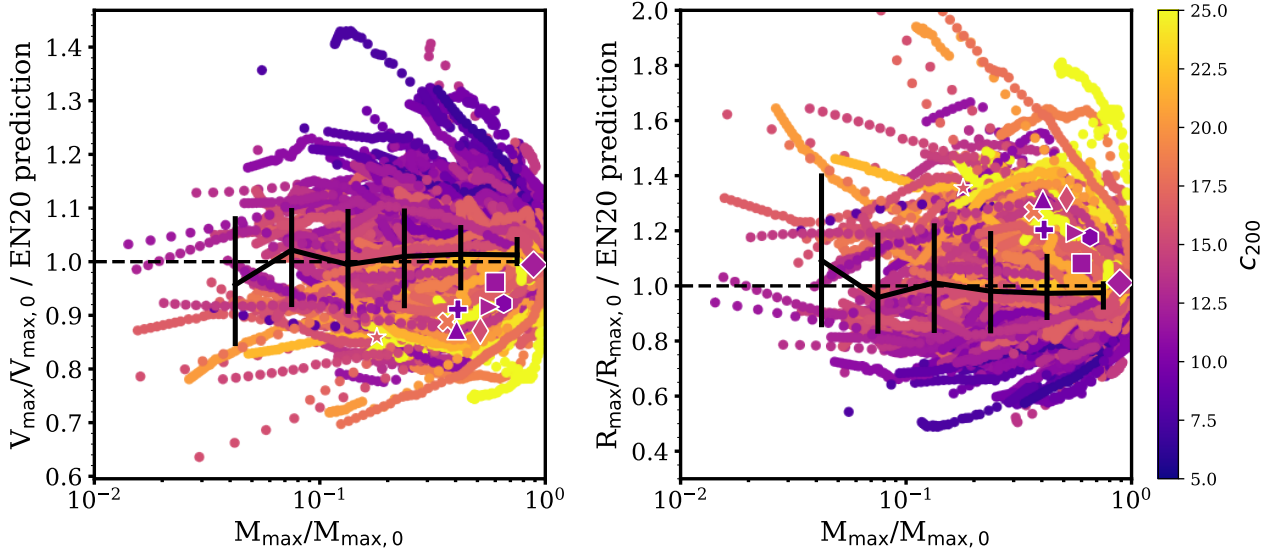


Figure B1. *Left:* fractional change in the maximum circular velocity, $V_{\max}/V_{\max,0}$, of our satellite dwarfs, divided by the fractional change predicted by [Errani & Navarro 2020](#) (EN20) for a given fraction of bound mass remaining within R_{\max} , $M_{\max}/M_{\max,0}$. For each satellite, we use multiple snapshots after infall, but we exclude those where the satellites come within 50 kpc of the host halo. The points are coloured by halo concentration, c_{200} . The error bars are the median and 1σ intervals in bins of $M_{\max}/M_{\max,0}$. The various symbols show our Fornax analogues. *Right:* as in the left panel, but the fractional change in the radius of the maximum circular velocity, $R_{\max}/R_{\max,0}$, compared to the predictions of [Errani & Navarro \(2020\)](#).